

Ultrafast endocytosis at mouse hippocampal synapses

Shigeki Watanabe¹, Benjamin R. Rost^{2†*}, Marcial Camacho-Pérez^{2*}, M. Wayne Davis¹, Berit Söhl-Kielczynski², Christian Rosenmund² & Erik M. Jorgensen¹

To sustain neurotransmission, synaptic vesicles and their associated proteins must be recycled locally at synapses. Synaptic vesicles are thought to be regenerated approximately 20 s after fusion by the assembly of clathrin scaffolds or in approximately 1 s by the reversal of fusion pores via ‘kiss-and-run’ endocytosis. Here we use optogenetics to stimulate cultured hippocampal neurons with a single stimulus, rapidly freeze them after fixed intervals and examine the ultrastructure using electron microscopy—‘flash-and-freeze’ electron microscopy. Docked vesicles fuse and collapse into the membrane within 30 ms of the stimulus. Compensatory endocytosis occurs within 50 to 100 ms at sites flanking the active zone. Invagination is blocked by inhibition of actin polymerization, and scission is blocked by inhibiting dynamin. Because intact synaptic vesicles are not recovered, this form of recycling is not compatible with kiss-and-run endocytosis; moreover, it is 200-fold faster than clathrin-mediated endocytosis. It is likely that ‘ultrafast endocytosis’ is specialized to restore the surface area of the membrane rapidly.

Recycling of synaptic vesicle membrane and proteins is required to keep membrane surface area constant and ensure efficient neurotransmission during sustained synaptic activity. Classical ultrastructural analysis of frog neuromuscular junctions led to two models of endocytosis. A slow endocytic pathway that takes place distant from active zones via clathrin scaffolds ~20 s after exocytosis was proposed¹. A fast mechanism, now termed kiss-and-run, that retrieves fusing vesicles by reversing their neck was then suggested^{2,3}—a process that takes place within 1 s^{4–6}. Since then, many studies have focused on understanding the molecular mechanisms and the kinetics of endocytosis to distinguish these two models. However, conflicting evidence has accumulated over the past 40 years.

The studies on the molecular mechanisms suggest that proteins associated with clathrin play crucial roles in synaptic vesicle endocytosis^{7,8}. Purified clathrin and its adaptor proteins are sufficient to reconstitute vesicles from brain-derived liposomes⁹. When cleavage by dynamin is disrupted, clathrin-coated pits and coated vesicles accumulate at the plasma membrane of synapses^{10,11}. Likewise, reductions of clathrin-interacting adaptor proteins^{12–15}, membrane-curvature proteins^{16–18} or scaffolding proteins^{19–21} perturb endocytosis at the synapse. On the other hand, the recruitment of clathrin triskelion is known to be very slow—on a time scale of seconds²², making it difficult to reconcile how vesicles can be regenerated when firing rates exceed 100 Hz²³. Moreover, functional vesicles are still regenerated in the absence of clathrin or its adaptor proteins^{13,24}, suggesting that another pathway may be operating at synapses.

The conclusions from studies on kinetics of endocytosis are often contradictory, but in some cases suggest that both kiss-and-run and clathrin-mediated endocytosis are operational at the synapse. Fluid-phase uptake of fluorescent dyes^{5,25,26} or measurements of open times using quantum dots^{4,27} show two kinetic components: fast (1–2 s) and slow (~20 s), although some authors have reported only a single kinetic component²⁸. Dye release of vesicles during exocytosis indicates that some dye is retained in the vesicle and suggests the presence of a

transient fusion pore that opens during kiss-and-run^{4,5,26}. Capacitance measurements from the calyx of Held²⁹, retinal bipolar cells⁶, and hippocampal mossy fibre boutons³⁰ suggest that both fast and slow mechanisms are probably at work. On the other hand, the measurement of protein trafficking using the pH-sensitive fluorescent protein pHluorin suggests that endocytosis of vesicle proteins in mammalian central synapses occurs with a single time constant of 15 s^{31,32}, similar to the time course revealed by ultrastructural analysis of the clathrin-mediated pathway¹.

The classic ultrastructural studies that gave rise to these models have certain caveats. For the cold-glutaraldehyde fixations, minutes- to hours-long stimulations were applied to dissected frog neuromuscular junctions^{1,2}. For the freeze-slammer experiments, 4-aminopyridine was applied to block potassium channels and prolong release^{3,33}. To observe synaptic ultrastructure following a single physiological stimulation, we developed a device that couples optogenetics and rapid high-pressure freezing³⁴. Using this ‘flash-and-freeze’ approach, we found that endocytosis occurs within 50 ms after stimulation at the edges of active zones in the nematode *Caenorhabditis elegans*³⁴. Here we applied a brief single light stimulus to mouse hippocampal neurons expressing channelrhodopsin and froze them at various time points ranging from 15 ms to 10 s after stimulation. Morphometry was conducted blind for 200 synapses from each time point. We found that endocytosis takes place between 50 and 100 ms after stimulation at the edge of active zones (Extended Data Fig. 1). These results indicate that ultrafast endocytosis mediated by actin and dynamin may be the first step in synaptic vesicle recycling in mouse hippocampal neurons.

Docked vesicles fuse in the active zone

To capture membrane dynamics during neurotransmission, we coupled optogenetics with high-pressure freezing of cultured mouse hippocampal neurons. Primary cultures were infected with lentivirus expressing channelrhodopsin-2 (E123T/T159C; hereafter ‘ChetaTC’)^{35,36}. On-cell electrophysiological recordings performed at 34 °C revealed that a single 10 ms pulse of blue light elicits at least one action potential with a mean

¹Department of Biology and Howard Hughes Medical Institute, University of Utah, Salt Lake City 84112, Utah, USA. ²Neuroscience Research Centre, Charité Universitätsmedizin, 10117 Berlin, Germany.

†Present address: German Center for Neurodegenerative Diseases (DZNE), 10117 Berlin, Germany.

*These authors contributed equally to this work.

delay of 4.8 ± 0.4 ms after light onset in 88% of the infected neurons (Fig. 1a and Extended Data Fig. 2). Some cells (20%, 7/34) fired a second action potential within 30 ms of light-on as illustrated in the sample trace (Fig. 1a). No action potential was observed in 12% of the cells (4/34; Extended Data Fig. 2b). Application of tetrodotoxin blocks light-evoked neurotransmitter release (Fig. 1b, upper trace), demonstrating that vesicle fusion is triggered by action potentials rather than by a global membrane depolarization by channelrhodopsin. Postsynaptic currents were observed with a delay of $\sim 6.9 \pm 0.3$ ms after light-on (Fig. 1b), and were blocked by NBQX and bicuculline (Fig. 1b, middle trace). In paired recordings of isolated ChetaTC positive and negative neurons, alternating light or electrical stimulation in the ChetaTC-positive cell elicits identical postsynaptic currents, demonstrating that in our conditions channelrhodopsin is acting solely via action potential generation, rather than supplementing calcium in the synaptic bouton (Extended Data Fig. 3).

To capture synaptic structures during neurotransmission, we applied a single 10-ms pulse of blue light, froze the cells using a high-pressure freezer at defined time points ranging from 15 ms up to 10 s after light onset, and prepared the samples for electron microscopy (Extended Data Fig. 2d, see Methods). To enhance release probability, the external solution contained 4 mM calcium. Omega figures of fusing vesicles were only rarely observed in unstimulated synapses (1% profiles with no stimulation, Fig. 1f), whereas they were found in 20% of synaptic profiles 15 ms after light onset (~ 10 ms after the initiation of an action potential). Thus, these structures probably represent fusions occurring during

peak transmission or phasic release (Fig. 1b). Fusions were observed within the active zone (Fig. 1c–e), and the diameters of these pits were similar to those of synaptic vesicles, and thus each pit represents the fusion of a single synaptic vesicle (Fig. 1g). Based on the wide opening at their neck (Fig. 1c–e), these pits are likely to be collapsing into the membrane, and the omega structures perdure for 20 ms ($\tau = 20.3$ ms, see Methods). Occasionally, multiple pits were observed in single sections (Fig. 1e), indicating that multi-vesicular release can occur in response to a single action potential or tightly spaced action potentials (20% of stimulated cells, Fig. 1a and Extended Data Fig. 2b). In either case, the presence of multiple fusing vesicles indicates that the fusion of a second vesicle is not blocked by the preceding fusion event.

We defined docked vesicles as those in direct contact with the membrane, in addition we scored vesicles with tethers that were within 30 nm of the plasma membrane (Fig. 2a). The number of docked vesicles was reduced from 1.7 to 1.0 per profile after the stimulus, but the tethered pool was largely unaffected (Fig. 2b–d). The docked pool recovered with a time constant of 3.8 s (Fig. 2b), which is similar to the time constant (4.3 s) for the recovery of the readily releasable pool previously measured in mouse hippocampal neurons by electrophysiology³⁷. These data indicate that docked vesicles are likely to be the morphological correlates of the physiologically defined readily-releasable pool.

Endocytosis peaks at 100 ms

Following exocytosis, endocytic structures appeared adjacent to the active zone (Fig. 3 and Fig. 4; Extended Data Fig. 4 for more example electron micrographs). Shallow pits (<40 nm), deep pits (>40 nm), and fully internalized vesicles (>50 nm) were all observed within 50 ms after stimulation and were declining by 300 ms (Fig. 3a–d, i). The number of shallow and deep pits increases again at 1 s, indicating a possible secondary wave of endocytosis. The diameters of these endocytic pits and large vesicles are similar (86 ± 2.4 nm and 82 ± 1.2 nm, respectively), suggesting a precursor–product relationship between these structures (Fig. 3h). The surface area of large vesicles is comparable to the surface area of about four synaptic vesicles (see membrane calculations in Methods). Electron-dense filaments are occasionally visible

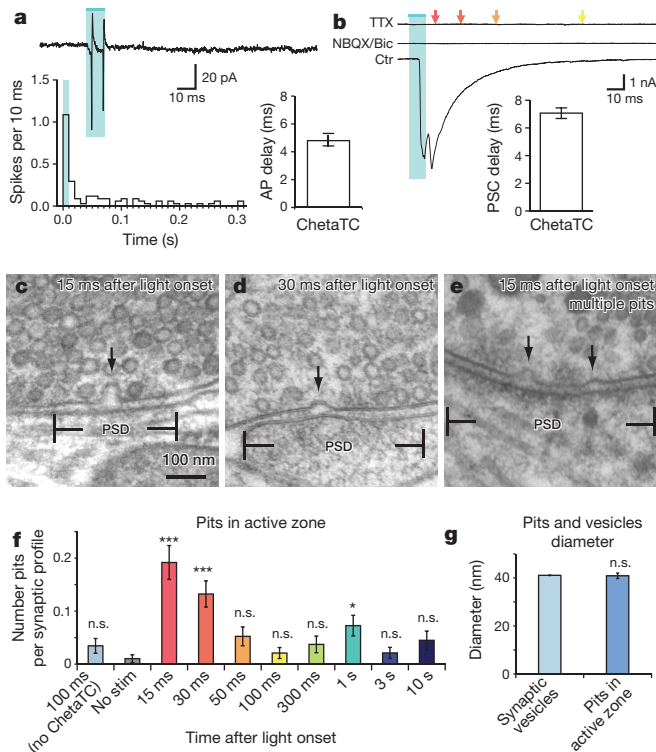


Figure 1 | Channelrhodopsin activation induces action-potential-driven vesicle fusion. **a**, Cell-attached voltage clamp recordings of light-evoked action potentials. The histogram shows the average number of action potentials (AP) at different time points after the light application. Each column is binned by 10 ms. **b**, Sample trace of light-evoked postsynaptic currents. Arrows indicate freezing times at 15, 30, 50, and 100 ms. **c**, **d**, Representative micrographs of fusing vesicles at 15 ms (**c**) and 30 ms (**d**) after the light onset. **e**, A micrograph showing two exocytic intermediates in the active zone. **f**, Average number of pits in the active zone at different time points after stimulation. **g**, Diameter of synaptic vesicles (41.1 ± 0.1 nm; $n = 382$) and pits in active zones (40.9 ± 1.2 nm; $n = 62$; $P = 0.7$). *** $P < 0.0001$; * $P < 0.006$. n.s., not significant. Error bars, s.e.m.

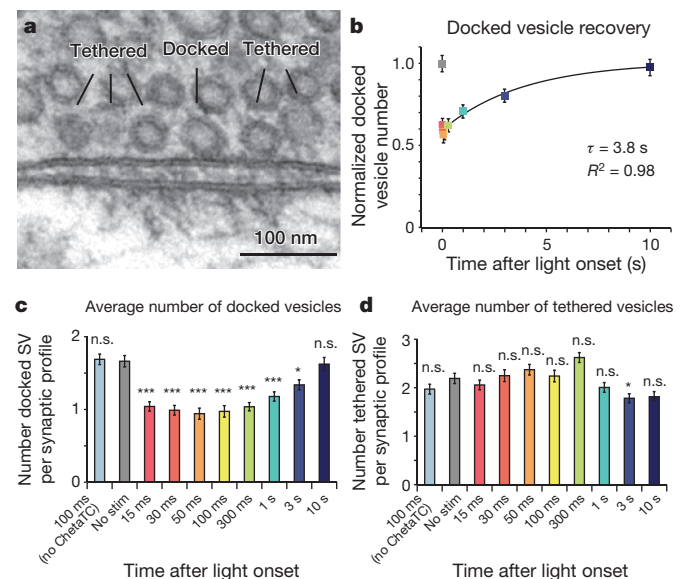


Figure 2 | Docked vesicles are the morphological correlates of the readily-releasable pool. **a**, A sample micrograph showing docked and tethered vesicles. **b**, Recovery of docked vesicles. The number of docked vesicles is normalized to the non-stimulated control (0 ms). The τ for recovery was 3.8 s. **c**, **d**, Average number of synaptic vesicles (SV) docked (**c**) or tethered (**d**) in the active zone at time points after the stimulus. For detailed numbers and statistical analysis, see Supplementary Table 1. *** $P < 0.0001$; * $P < 0.006$. n.s., not significant. Error bars, s.e.m.

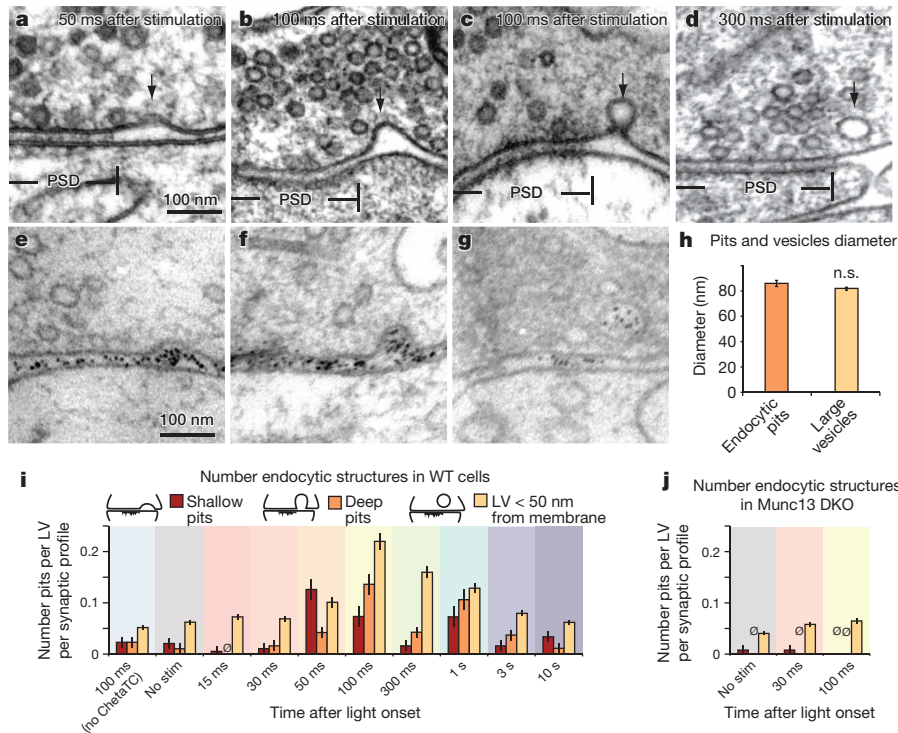


Figure 3 | Large invaginations immediately next to the active zone are endocytic intermediates. **a–d**, Representative micrographs showing invaginations and large vesicles in the periactive zone at 50 ms (**a**), 100 ms (**b, c**) and 300 ms (**d**) after stimulation. **e–g**, Sample micrographs showing ferritin uptake into these large endocytic structures at 100 ms after stimulation. **h**, Diameter of large vesicles (82.0 ± 1.2 nm; $n = 572$) and endocytic invaginations (86.0 ± 2.4 nm; $n = 51$; $P = 0.33$). **i**, Number of

shallow pits (<40 nm), deep pits (>40 nm), and large vesicles (LV; <50 nm from plasma membrane) in the periactive zone at different time points after stimulation. **j**, Number of shallow pits, deep pits and large vesicles in the periactive zone at different time points after stimulation in Munc13 DKO. For detailed numbers and statistical analysis, see Supplementary Table 1. n.s., not significant. Error bars, s.e.m.

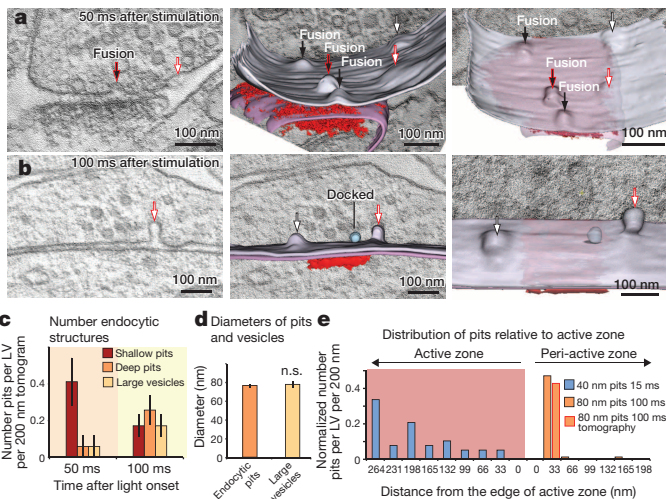


Figure 4 | Endocytosis is localized to sites flanking the active zone. **a, b**, Tomograms of synapses frozen 50 ms (**a**) or 100 ms (**b**) after stimulation. Left, a virtual 2 nm section from the tomograms. Middle, orthogonal views of the reconstructed volumes. Right, tilted views of the reconstructed volumes. The postsynaptic density is coloured red to delineate the extent of the active zone. Black and white arrows indicate fusing vesicles and endocytic pits, respectively. Arrows outlined in red indicate the plane of the image shown in the left panels. **c**, Number of shallow pits, deep pits and large vesicles in the periactive zone at different time points after stimulation. **d**, Diameter of large vesicles (78.0 ± 3.3 nm; $n = 6$) and endocytic invaginations (76.3 ± 1.9 nm; $n = 15$; $P = 0.56$). **e**, Distribution of pits relative to the edge of active zone. For detailed numbers and statistical analysis, see Supplementary Table 1. n.s., not significant. Error bars, s.e.m.

around these endocytic structures (Extended Data Fig. 4j, k), but they differ from classical coats (Extended Data Fig. 4m–p).

To confirm the spatial relationship of exocytic and endocytic sites, we performed electron tomography on 200-nm thick sections at 50 ms and 100 ms after stimulation (Fig. 4). Fusing vesicles, defined by their diameter, were rare and were not observed in the 100-ms tomograms (Fig. 4a). Endocytic invaginations were outside the active zone and were often observed flanking the active zone (Fig. 4b, e). The number of shallow invaginations declines at 100 ms and is associated with an increase in the number of deep pits and large vesicles (Fig. 4c) similar to the 40-nm sections (Fig. 3i). The diameters of pits (76.3 ± 1.9 nm) and large vesicles (78.0 ± 3.3 nm) are similar, again suggesting a precursor–product relationship (Fig. 4d).

One potential interpretation of these data is that synaptic vesicles first undergo homotypic compound fusion to generate a large vesicle^{38,39}, and then fuse to the plasma membrane. To exclude such a possibility we used ferritin as a fluid phase marker to label endocytic structures. Cationized ferritin binds to negative charges on the plasma membrane and becomes internalized by endocytosis. Ferritin-positive synaptic vesicles were only rarely observed in the absence of stimulation (Extended Data Fig. 5a; control no stimulation, see Methods). Cells were stimulated with a single light pulse and frozen 100 ms later. After stimulation, ferritin was found in invaginations (22% of the synapses) and large vesicles (16% of the synapses; Fig. 3e–g and Extended Data Fig. 5c–e for more example micrographs). The frequencies of endocytic structures were similar to matched controls with no ferritin, thus ferritin itself did not affect ultrafast endocytosis (Extended Data Fig. 5f, g). The presence of ferritin in large vesicles but not synaptic vesicles (Extended Data Fig. 5b) indicates that these large structures are due to endocytosis rather than compound fusion, and further indicates that synaptic vesicles are not being regenerated directly from the membrane on this time scale.

Ultrafast endocytosis scales with exocytosis

Some data suggest that calcium influx may be able to stimulate endocytosis without vesicle fusion⁴⁰. To test if calcium influx alone can stimulate ultrafast endocytosis, we repeated the experiment in cultured neurons from Munc13-1 Munc13-2 double mutants (Munc13-1/2 DKO), which should still experience calcium influx but lack synaptic vesicle exocytosis at hippocampal synapses^{41,42}. We applied a single light pulse to Munc13-1/2 DKO hippocampal neurons expressing ChetaTC and froze the sample at 0 ms, 30 ms and 100 ms. The number of docked vesicles was significantly reduced as previously observed^{41,42}, and no exocytic omega structures were observed. Endocytic structures were completely absent in Munc13-1/2 DKO cells (Fig. 3j). Thus, ultrafast endocytosis requires the addition of membrane to the surface via exocytosis and is not solely driven by calcium.

Nevertheless, increasing calcium is known to accelerate endocytosis during synaptic activity⁴³. In our experiments we used 4 mM calcium to increase release probability; it is possible that ultrafast endocytosis depends on elevated intracellular calcium. We therefore repeated the experiments using 2 mM calcium in the external solution (Extended Data Fig. 6). At least one action potential during the light pulse was observed in 73% of cells (11/15; Extended Data Fig. 6a, b). Endocytic intermediates were captured at the lateral edge of active zone 100 ms after stimulation (Extended Data Fig. 6c–e). The number of exocytic events and endocytic events was lower than the number observed with 4 mM calcium (Extended Data Fig. 6f, g). However, the kinetics of endocytosis were not altered. These results indicate that ultrafast endocytosis occurs under physiological conditions, but scales with the amount of membrane added by exocytosis.

To determine if ultrafast endocytosis can fully compensate for membrane added during exocytosis, we compared the surface area added by exocytosis to that removed by endocytosis (see Methods). The number of fused vesicles was determined by comparing docked vesicles at the 0 ms and 15 ms time points. We calculated that 3,700 nm² of membrane was added to the surface per each profile. The amount of membrane endocytosed at 100 ms was 3,150 nm². In short, we observe that 0.7 synaptic vesicles fuse per profile and 0.6 vesicle equivalents are recovered per profile. These data indicate that a majority of the membrane added by full-collapse fusion after a single stimulus is retrieved by ultrafast endocytosis.

Actin and dynamin mediate endocytosis

Some forms of endocytosis, either clathrin-dependent or -independent, are mediated by actin⁴⁴. To investigate the role of actin polymerization in ultrafast endocytosis, we applied latrunculin-A (Fig. 5), which disrupts polymerization of actin⁴⁵. Application of 0.1% dimethylsulphoxide (DMSO) or 10 μ M latrunculin-A for 1 min did not affect evoked neurotransmission (Fig. 5d and Extended Data Fig. 7a, b). Hippocampal neurons treated with either latrunculin-A or DMSO for 30 s were frozen 100 ms after light stimulation (Fig. 5a, b and Extended Data Fig. 7c–h for more representative micrographs). The DMSO-treated neurons showed normal endocytosis (Fig. 5b, e). No endocytic structures were observed in the latrunculin-A treated cells (Fig. 5a, e), indicating that polymerized actin is required for ultrafast endocytosis.

Cleavage of budded vesicles from the plasma membrane is associated with the GTPase dynamin^{10,11}. Dynasore is a small molecule that interferes with the GTPase activity of dynamin and blocks the cleavage of membrane necks⁴⁶, but may also affect the actin cytoskeleton⁴⁷. We applied 80 μ M dynasore for 30 s before freezing. Unstimulated neurons treated with dynasore did not accumulate pits, indicating that spontaneous activity does not contribute substantially to trapped endocytic intermediates (Fig. 5f; 0.1 pits or large vesicles per profile in both treated and control). In cultures stimulated by a single pulse of light and frozen 100 ms later, dynasore treatment did not increase the total number of endocytic structures, indicating that dynasore did not increase exocytosis and thereby indirectly increase endocytic structures (Fig. 5f; 0.4 endocytic structures per profile in treated and control). However, the

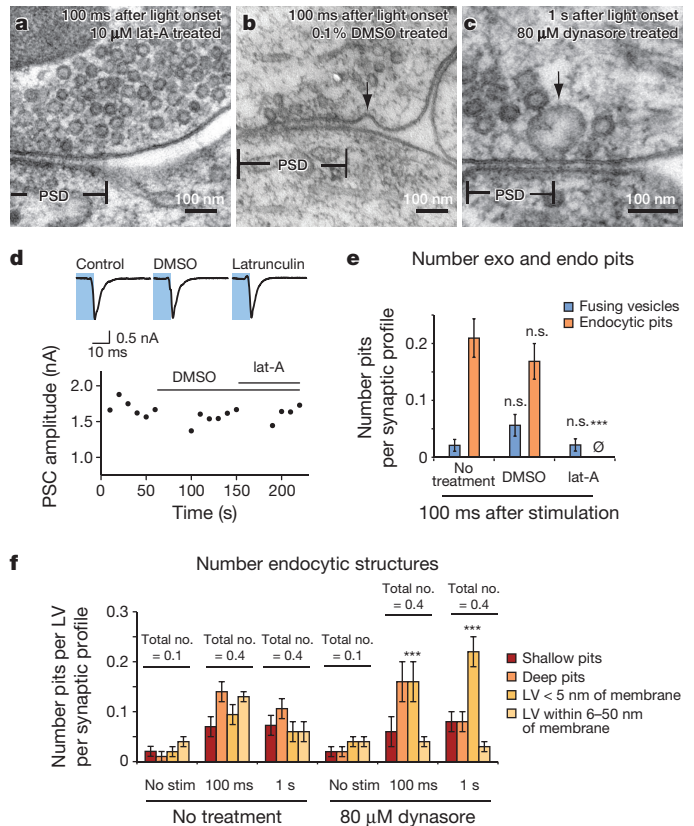


Figure 5 | Ultrafast endocytosis is mediated by actin and dynamin.

a, b, Representative micrographs showing 10 μ M latrunculin-A (**a**) and 0.1% DMSO (**b**) 100 ms after light stimulation. **c**, A representative micrograph showing 80 μ M dynasore-treated cells 1 s after light stimulation. **d**, Traces of average postsynaptic currents in the absence of drugs, during the DMSO application, and during the latrunculin-A application. **e**, Average number of exocytic pits (blue) and endocytic pits (orange) in the latrunculin-A- or DMSO-treated cells. **f**, Number of shallow pits, deep pits and large vesicles associated with the membrane (<5 nm) and large vesicles associated with the active zone (6–50 nm of the membrane). Controls are from the samples in Fig. 3. For detailed numbers and statistical analysis, see Supplementary Table 1. *** $P < 0.0001$. n.s., not significant. Error bars, s.e.m.

fraction of structures remaining as large vesicles trapped close to the membrane increased (Fig. 5f; control: 0.09 large vesicles per profile, treated: 0.16 large vesicles). By 1 s after stimulation, the endocytic structures had progressed to large vesicles, but remained associated with the membrane in dynasore-treated samples (control: 0.06 large vesicles, treated: 0.22 large vesicles; Fig. 5c, f and Extended Data Fig. 8a–c for more micrographs). Necks were only visible in 18% of the trapped large vesicles (10/57), possibly due to the thickness of the sections (40 nm). Electron tomography revealed that the large vesicles were still attached to the membrane (Extended Data Fig. 8d–f), indicating that these large vesicles are trapped on the surface. Together, these results indicate that endocytosis in hippocampal neurons occurs within 100 ms lateral to the active zone, and is mediated by actin polymerization and dynamin.

Discussion

It is widely agreed that after high-frequency stimulation, membranes and proteins are retrieved by clathrin^{7,48}. The best estimates for the speed of clathrin-mediated endocytosis at the synapse come from vesicle proteins tagged with pHluorin. Synaptic vesicle proteins freshly added to the surface after a single action potential are recycled with a time constant of about 15–20 s^{31,32}. In addition, a fraction of vesicle proteins already reside on the plasma membrane and are only endocytosed after stimulation⁴⁹. This readily retrievable pool of proteins is also internalized with a time constant of about 20 s after stimulation⁴⁹. Endocytosis

of synaptic vesicle proteins requires clathrin and clathrin adaptors and is probably specialized to bind and recover synaptic vesicle proteins lost to the plasma membrane³². These rates are slow compared to ultrafast endocytosis, which is 200 times faster, but the assembly kinetics of clathrin are known to be slow²². It is too premature to eliminate a role for clathrin in ultrafast endocytosis; the absence of distinctive clathrin coats does not exclude a role for clathrin in ultrafast endocytosis.

There is a large body of evidence for a fast pathway attributed to kiss-and-run endocytosis^{5,25,26}. Ultrafast endocytosis is not kiss-and-run because of three characteristics: first, the vesicle fusions we observe have broad openings, suggesting they are collapsing into the membrane. Second, ultrafast endocytosis takes place at the lateral edge of the active zone, rather than in the middle of the active zone where fusion takes place. Third, the surface area of the invaginations is equivalent to four synaptic vesicles rather than one vesicle. It is unlikely that these large vesicles represent the recovery of intact synaptic vesicles.

Nevertheless, kiss-and-run events should be captured in our preparation, because they are thought to be more abundant during low-frequency stimulation², and the pore is estimated to last approximately 1–2 s⁵. Thus kiss-and-run vesicles should be visible in the preparation at all time points between 15 ms and 1 s. However, the pore is estimated to be only 1–2 nm in diameter^{2,5}. Although such a pore has been observed previously by electron microscopy^{2,3}, such small structures would be difficult to observe routinely in 40-nm thick sections. We cannot exclude the possibility of kiss-and-run figures in our micrographs. However, it is unlikely that kiss-and-run constitutes a significant fraction of endocytic events in our preparation: presumably kiss-and-run vesicles would become undocked after stimulation, and our calculations of membrane surface area suggest that ultrafast endocytosis can account for most docked vesicles lost to fusion after a single stimulus.

Ultrafast endocytosis is likely to be an evolutionarily conserved process. At the frog neuromuscular junction, depressions adjacent to the active zone were observed in freeze-fracture studies 1 s after stimulation³³; these depressions were interpreted as a potentially fast form of endocytosis. Capacitance measures in retinal bipolar cells indicate that a fast form of endocytosis ($\tau = 1$ s) is clathrin-independent⁶. Ultrastructural studies at *C. elegans* neuromuscular junctions indicate that endocytosis can be as fast as 50 ms following a single stimulus and also occurs at the lateral edges of the active zone³⁴. The data presented here suggest that ultrafast endocytosis almost instantaneously compensates for membrane added to the plasma membrane. The rapid communication between fusion in the active zone and the endocytic sites at the lateral edges is probably mediated by a relaxation in membrane tension. The intriguing unknown is how membrane tension could be coupled to the endocytic machinery.

METHODS SUMMARY

Mouse hippocampal neurons were cultured on astrocyte feeder layers in mass cultures. Cells were infected using lentivirus expressing channelrhodopsin-2 (E123T/T159C). Experiments were performed after 13–15 days in culture. Action potentials were recorded in the cell-attached voltage clamp configuration after a single 10-ms light stimulus in 34 °C HEPES-buffered solution containing 4 mM Ca²⁺, 1 mM Mg²⁺, 3 μ M NBQX and 30 μ M bicuculline.

For measuring synaptic delay and effects of latrunculin-A, we infected 20% of cells with mKate and 80% of cells with ChetaTC, co-cultured the infected cells, and patched mKate-positive cells that lacked photocurrents. Whole-cell patch clamp recordings were conducted at 34 °C in the absence of NBQX or bicuculline.

For electron microscopy, neurons were grown on 6-mm sapphire disks. The neurons were transferred into the same extracellular solutions ~30 s before freezing. A single 10-ms light pulse was applied at defined time points before high-pressure freezing. Following freeze-substitution, en bloc staining with uranyl acetate and plastic embedding, serial 40-nm sections were collected. The samples were blinded before imaging and analysis. Approximately 200 synaptic profiles were randomly chosen from each time point and analysed blind.

For electron tomography, 200-nm thick sections were collected. Tilt series of $\pm 65^\circ$ were acquired, and tomograms generated using IMOD. Membranes were segmented using Amira or TrakEM2.

For ferritin uptake experiments, cells were immersed in solution containing 0.25 mg ml⁻¹ ferritin for 5 min in reduced external calcium solution (1 mM) to suppress spontaneous activity. For latrunculin-A and dynasore experiments, we applied a solution containing 10 μ M latrunculin or 80 μ M dynasore or 0.1% DMSO 30 s before stimulation and freezing.

For a complete description of statistical tests, see Supplementary Table 1. For detailed description of methods and membrane calculations, see Methods.

Online Content Any additional Methods, Extended Data display items and Source Data are available in the online version of the paper; references unique to these sections appear only in the online paper.

Received 7 June; accepted 1 November 2013.

Published online 4 December 2013.

- Heuser, J. E. & Reese, T. S. Evidence for recycling of synaptic vesicle membrane during transmitter release at the frog neuromuscular junction. *J. Cell Biol.* **57**, 315–344 (1973).
- Ceccarelli, B., Hurlbut, W. P. & Mauro, A. Depletion of vesicles from frog neuromuscular junctions by prolonged tetanic stimulation. *J. Cell Biol.* **54**, 30–38 (1972).
- Torri-Tarelli, F., Grohovaz, F., Fesce, R. & Ceccarelli, B. Temporal coincidence between synaptic vesicle fusion and quantal secretion of acetylcholine. *J. Cell Biol.* **101**, 1386–1399 (1985).
- Zhang, Q., Cao, Y.-Q. & Tsien, R. W. Quantum dots provide an optical signal specific to full collapse fusion of synaptic vesicles. *Proc. Natl Acad. Sci. USA* **104**, 17843–17848 (2007).
- Richards, D. A., Bai, J. & Chapman, E. R. Two modes of exocytosis at hippocampal synapses revealed by rate of FM1-43 efflux from individual vesicles. *J. Cell Biol.* **168**, 929–939 (2005).
- Von Gersdorff, H. & Matthews, G. Dynamics of synaptic vesicle fusion and membrane retrieval in synaptic terminals. *Nature* **367**, 735–739 (1994).
- Dittman, J. & Ryan, T. A. Molecular circuitry of endocytosis at nerve terminals. *Annu. Rev. Cell Dev. Biol.* **25**, 133–160 (2009).
- Maycox, P. R., Link, E., Reetz, A., Morris, S. A. & Jahn, R. Clathrin-coated vesicles in nervous tissue are involved primarily in synaptic vesicle recycling. *J. Cell Biol.* **118**, 1379–1388 (1992).
- Takei, K. *et al.* Generation of coated intermediates of clathrin-mediated endocytosis on protein-free liposomes. *Cell* **94**, 131–141 (1998).
- Koenig, J. H. & Ikeda, K. Disappearance and reformation of synaptic vesicle membrane upon transmitter release observed under reversible blockage of membrane retrieval. *J. Neurosci.* **9**, 3844–3860 (1989).
- Shupliakov, O. *et al.* Synaptic vesicle endocytosis impaired by disruption of dynamin-SH3 domain interactions. *Science* **276**, 259–263 (1997).
- Gu, M. *et al.* AP2 hemicomplexes contribute independently to synaptic vesicle endocytosis. *eLife* **2**, e00190 (2013).
- Kim, S. H. & Ryan, T. A. Synaptic vesicle recycling at CNS synapses without AP-2. *J. Neurosci.* **29**, 3865–3874 (2009).
- Nonet, M. L. *et al.* UNC-11, a *Caenorhabditis elegans* AP180 homologue, regulates the size and protein composition of synaptic vesicles. *Mol. Biol. Cell* **10**, 2343–2360 (1999).
- Diril, M. K., Wienisch, M., Jung, N., Klingauf, J. & Haucke, V. Stonin 2 is an AP-2-dependent endocytic sorting adaptor for synaptotagmin internalization and recycling. *Dev. Cell* **10**, 233–244 (2006).
- Schmidt, A. *et al.* Endophilin I mediates synaptic vesicle formation by transfer of arachidonate to lysophosphatidic acid. *Nature* **401**, 133–141 (1999).
- Verstreken, P. *et al.* Endophilin mutations block clathrin-mediated endocytosis but not neurotransmitter release. *Cell* **109**, 101–112 (2002).
- Anggono, V. *et al.* Syndapin I is the phosphorylation-regulated dynamin I partner in synaptic vesicle endocytosis. *Nature Neurosci.* **9**, 752–760 (2006).
- Jakobsson, J. *et al.* Role of epsin 1 in synaptic vesicle endocytosis. *Proc. Natl Acad. Sci. USA* **105**, 6445–6450 (2008).
- Koh, T.-W., Verstreken, P. & Bellen, H. J. Dap160/intersectin acts as a stabilizing scaffold required for synaptic development and vesicle endocytosis. *Neuron* **43**, 193–205 (2004).
- Marie, B. *et al.* Dap160/intersectin scaffolds the periaxial zone to achieve high-fidelity endocytosis and normal synaptic growth. *Neuron* **43**, 207–219 (2004).
- Cocucci, E., Aguet, F., Boulant, S. & Kirchhausen, T. The first five seconds in the life of a clathrin-coated pit. *Cell* **150**, 495–507 (2012).
- Maeno-Hikichi, Y., Polo-Parada, L., Kastanenka, K. V. & Landmesser, L. T. Frequency-dependent modes of synaptic vesicle endocytosis and exocytosis at adult mouse neuromuscular junctions. *J. Neurosci.* **31**, 1093–1105 (2011).
- Sato, K. *et al.* Differential requirements for clathrin in receptor-mediated endocytosis and maintenance of synaptic vesicle pools. *Proc. Natl Acad. Sci. USA* **106**, 1139–1144 (2009).
- Teng, H., Cole, J. C., Roberts, R. L. & Wilkinson, R. S. Endocytic active zones: hot spots for endocytosis in vertebrate neuromuscular terminals. *J. Neurosci.* **19**, 4855–4866 (1999).
- Harata, N. C., Choi, S., Pyle, J. L., Aravanis, A. M. & Tsien, R. W. Frequency-dependent kinetics and prevalence of kiss-and-run and reuse at hippocampal synapses studied with novel quenching methods. *Neuron* **49**, 243–256 (2006).
- Park, H., Li, Y. & Tsien, R. W. Influence of synaptic vesicle position on release probability and exocytotic fusion mode. *Science* **335**, 1362–1366 (2012).
- Ryan, T. A., Smith, S. J. & Reuter, H. The timing of synaptic vesicle endocytosis. *Proc. Natl Acad. Sci. USA* **93**, 5567–5571 (1996).

29. Renden, R. & von Gersdorff, H. Synaptic vesicle endocytosis at a CNS nerve terminal: faster kinetics at physiological temperatures and increased endocytotic capacity during maturation. *J. Neurophysiol.* **98**, 3349–3359 (2007).
30. Hallermann, S., Pawlu, C., Jonas, P. & Heckmann, M. A large pool of releasable vesicles in a cortical glutamatergic synapse. *Proc. Natl Acad. Sci. USA* **100**, 8975–8980 (2003).
31. Balaji, J. & Ryan, T. A. Single-vesicle imaging reveals that synaptic vesicle exocytosis and endocytosis are coupled by a single stochastic mode. *Proc. Natl Acad. Sci. USA* **104**, 20576–20581 (2007).
32. Granseth, B., Odermatt, B., Royle, S. J. & Lagnado, L. Clathrin-mediated endocytosis is the dominant mechanism of vesicle retrieval at hippocampal synapses. *Neuron* **51**, 773–786 (2006).
33. Miller, T. M. & Heuser, J. E. Endocytosis of synaptic vesicle membrane at the frog neuromuscular junction. *J. Cell Biol.* **98**, 685–698 (1984).
34. Watanabe, S. *et al.* Ultrafast endocytosis at *Caenorhabditis elegans* neuromuscular junctions. *eLife* **2**, e00723 (2013).
35. Gunaydin, L. A. *et al.* Ultrafast optogenetic control. *Nature Neurosci.* **13**, 387–392 (2010).
36. Berndt, A. *et al.* High-efficiency channelrhodopsins for fast neuronal stimulation at low light levels. *Proc. Natl Acad. Sci. USA* **108**, 7595–7600 (2011).
37. Pyott, S. J. & Rosenmund, C. The effects of temperature on vesicular supply and release in autaptic cultures of rat and mouse hippocampal neurons. *J. Physiol.* **539**, 523–535 (2002).
38. Matthews, G. & Sterling, P. Evidence that vesicles undergo compound fusion on the synaptic ribbon. *J. Neurosci.* **28**, 5403–5411 (2008).
39. He, L. *et al.* Compound vesicle fusion increases quantal size and potentiates synaptic transmission. *Nature* **459**, 93–97 (2009).
40. Neale, E. A., Bowers, L. M., Jia, M., Bateman, K. E. & Williamson, L. C. Botulinum neurotoxin A blocks synaptic vesicle exocytosis but not endocytosis at the nerve terminal. *J. Cell Biol.* **147**, 1249–1260 (1999).
41. Varoqueaux, F. *et al.* Total arrest of spontaneous and evoked synaptic transmission but normal synaptogenesis in the absence of Munc13-mediated vesicle priming. *Proc. Natl Acad. Sci. USA* **99**, 9037–9042 (2002).
42. Siksou, L. *et al.* A common molecular basis for membrane docking and functional priming of synaptic vesicles. *Eur. J. Neurosci.* **30**, 49–56 (2009).
43. Armbruster, M., Messa, M., Ferguson, S. M., De Camilli, P. & Ryan, T. A. Dynamin phosphorylation controls optimization of endocytosis for brief action potential bursts. *eLife* **2**, e00845 (2013).
44. Mooren, O. L., Galletta, B. J. & Cooper, J. A. Roles for actin assembly in endocytosis. *Annu. Rev. Biochem.* **81**, 661–686 (2012).
45. Spector, I., Shochet, N. R., Kashman, Y. & Groweiss, A. Latrunculins: novel marine toxins that disrupt microfilament organization in cultured cells. *Science* **219**, 493–495 (1983).
46. Macia, E. *et al.* Dynasore, a cell-permeable inhibitor of dynamin. *Dev. Cell* **10**, 839–850 (2006).
47. Yamada, H. *et al.* Dynasore, a dynamin inhibitor, suppresses lamellipodia formation and cancer cell invasion by destabilizing actin filaments. *Biochem. Biophys. Res. Commun.* **390**, 1142–1148 (2009).
48. McMahon, H. T. & Boucrot, E. Molecular mechanism and physiological functions of clathrin-mediated endocytosis. *Nature Rev. Mol. Cell Biol.* **12**, 517–533 (2011).
49. Wienisch, M. & Klingauf, J. Vesicular proteins exocytosed and subsequently retrieved by compensatory endocytosis are nonidentical. *Nature Neurosci.* **9**, 1019–1027 (2006).

Supplementary Information is available in the online version of the paper.

Acknowledgements We would like to thank D. Lorenz and A. Muenster-Wandowski for providing access to electron microscopes. We would like to thank P. Hegemann and F. Schneider for providing the ChetaTC construct, A. Felies for cell cultures, B. Brokowski for generating lentivirus, E. Hujber for image processing and freezing calculations, C. Ebeling for calculating the time constant for synaptic vesicle collapse, and J. Iwasa for drawing the model figure. We would like to thank C. Tomova and Leica Microsystems for providing us with technical details of the controller of the high-pressure freezer for precise temporal control of light stimulation. We thank EMBO for providing the travel funds (S.W.). The research was funded by the US National Institutes of Health (NS034307; E.M.J.), European Research Council grant (249939 SYNGLUT; C.R.), and German Research Council grants (EXC 257, SFB 665, SFB958; C.R.). E.M.J. is an Investigator of the Howard Hughes Medical Institute and is an Alexander von Humboldt Scholar.

Author Contributions S.W., C.R., and E.M.J. conceived and designed experiments. M.W.D. designed and programmed the light device. S.W. and B.S.-K. performed the freezing experiments. B.R.R. designed lentivirus constructs. B.R.R. and M.C.-P. performed electrophysiology. S.W. performed electron microscopy imaging and analysis. S.W., B.R.R., M.C.-P., C.R. and E.M.J. wrote the manuscript. C.R. and E.M.J. provided funding. experiments were performed at the Charité Universitätsmedizin, Berlin, Germany.

Author Information Reprints and permissions information is available at www.nature.com/reprints. The authors declare no competing financial interests. Readers are welcome to comment on the online version of the paper. Correspondence and requests for materials should be addressed to E.M.J. (jorgensen@biology.utah.edu) and C.R. (christian.rosenmund@charite.de).

METHODS

Cell cultures and lentivirus infection. Animals were handled according to the rules of Berlin authorities and the animal welfare committee of the Charité Berlin, Germany. Newborn C57/BL6-N mice were decapitated and brains quickly transferred into cold HBSS. For feeder layer cultures, cortices were treated with trypsin for 20 min, triturated and seeded into T-75 flasks containing DMEM supplemented with 10% FCS and 0.1% penicillin-streptomycin. After 2 weeks, astrocytes were plated onto 6 mm sapphire disks (Wohlgend GmbH) for high pressure freezing experiments or 15 mm glass coverslips (Hecht Assistant) for electrophysiology. Hippocampi were dissected under a binocular and digested using papain for 1 h at 37 °C. After trituration, neurons were seeded onto astrocyte feeder layers at densities of $13 \times 10^3 \text{ cm}^{-2}$ in 12-well plates. Prior to addition of hippocampal neurons, culture medium was changed to Neurobasal-A supplemented with 2% B27, 0.1% penicillin-streptomycin (NB-A full medium, Invitrogen).

Virus production was performed as described previously⁵⁰. Briefly, HEK293T cells were transfected in T-75 flasks with a plasmid encoding channelrhodopsin-2 (E123T/T159C; ChetaTC) under control of a neuron-specific synapsin promoter, and the helper plasmids pCMVdr8.9 and pVSV.G (5 µg each) with X-tremeGENE 9 DNA transfection reagent (Roche). These modifications to channelrhodopsin-2 increase the maximal current and off-kinetics of the light-activated channel^{35,56}. Cultures were maintained in NB-A full medium in an incubator at 32 °C and 5% CO₂ for 72 h. Supernatant was harvested, filtered, concentrated to 500 µl using Amicon Ultra-15 centrifugal 10 kDa filter units and shock-frozen in liquid nitrogen. 25 µl of concentrated virus was used to transduce neurons at DIV1-2. Infection rates reached 100%, as monitored by yellow fluorescence protein (YFP) fluorescence and whole-cell current-clamp recordings.

For electrophysiological experiments using co-cultures of ChetaTC-positive and -negative cells, one set of hippocampal neurons was cultured as described above and infected 6–24 h post seeding. A new set of neurons was prepared 2–4 days later and incubated for 2–3 h in suspension with a lentivirus encoding mKate2. Subsequently, neurons were washed twice with NB-A full medium to remove viral particles, and added at low concentrations to the neurons expressing ChetaTC. For paired recordings on co-cultures of ChetaTC positive and negative neurons, we modified protocols for autaptic neuronal cultures⁵¹. In six-well plates, hippocampal neurons were seeded at low density (260 cells cm⁻²) on astrocyte microislands of 500-µm diameter and infected with ChetaTC virus. After 3 days, culture medium was changed, and uninfected striatal neurons were added at same concentration.

Electrophysiology. Whole-cell patch-clamp and cell-attached voltage-clamp mode recordings were performed under conditions mimicking the high-pressure freezing experiment. The extracellular solution contained (in mM): 140 NaCl, 2.4 KCl, 10 HEPES, 10 glucose, 4 CaCl₂, and 1 MgCl₂ (pH adjusted to 7.3 with NaOH, 300 mOsm). All recordings were performed at 34 °C using a Multiclamp 700B amplifier (Molecular Devices) under the control of Clampex 10.0 (Molecular Devices). Data was acquired at 10 kHz and filtered at 3 kHz. Intracellular solution for whole cell recordings contained (in mM): 146 K-gluconate (paired recordings) or KCl (mass cultures), 17.8 HEPES, 1 EGTA, 4 Mg-ATP, 0.3 Na-GTP, 12 creatine phosphate, 50 units ml⁻¹ creatine-phosphokinase (pH adjusted to 7.3 with KOH). Pipette resistance was 3–5 MΩ, and access resistance was compensated by 70%. Pipettes contained extracellular solution for cell-attached measurements of action-potentials evoked by light stimulation. Optical stimulation was provided by a 470 nm LED coupled into the fluorescence port of the microscope (Olympus-IX51), and triggered by a transistor-transistor logic (TTL) signal. The delay between TTL-trigger and light-onset is approximately 200 µs. For our morphological studies, each cell only received one light stimulus before freezing, and thus, in the cell attached recordings we recorded from cells that never experienced light stimulation before, and only applied one light pulse to each cell. Occasionally, multiple action potentials were observed during the 10 ms application of blue light as illustrated in the sample trace. An action potential was observed during the light pulse in 88% of the cells (30/34). Mean delay was 4.8 ± 0.4 ms after light-on. Postsynaptic responses follow $\sim 6.9 \pm 0.3$ ms after the initiation of the light stimulus (postsynaptic onset measured at 10% peak current, $n = 27$) in a ChetaTC-negative neuron, receiving synaptic input from a ChetaTC-positive neuron. The responses were blocked either by tetrodotoxin or by NBQX and bicuculline.

For testing the effect of latrunculin-A on evoked release, we recorded from mKate2-positive cells that did not express ChetaTC (Extended Data Fig. 7a). We measured light-evoked postsynaptic currents PSCs 4–6 times to calculate the average PSC amplitude. After 6 pulses of blue light at 0.1 Hz under control conditions, we applied 0.1% DMSO for 30 s and recorded PSCs with the same stimulation protocol. Finally, 10 µM latrunculin-A was applied for 30 s, and 4–6 PSCs were measured.

Electron microscopy. Cultured cells on sapphire disks were frozen using the HPM 100 high-pressure freezer (Leica) with an integrated light stimulation device. To achieve millisecond temporal control of light application, we built a device that triggers both light and freezing. We set the device so that a light stimulus is applied

at 15 ms, 30 ms, 50 ms, 100 ms, 300 ms, 1 s, 3 s and 10 s before freezing. The cells were mounted in the specimen mounts at room temperature, which typically requires 30 s to 1 min, but were recovered to 34 °C in the chamber before freezing.

Endocytosis should stop when the tissue reaches 0 °C. Leica has placed a thermometer inside their sample cup for the HPM100 and have measured a cooling rate of $6,000 \text{ K s}^{-1}$, which predicts that the sample would reach 0 °C in 6 ms. We cannot monitor the temperature of the sample, the high pressure freezer can only send telemetry concerning the temperature of the freezing chamber. In our instrument, the chamber reaches 0 °C 7 ms after the chamber is flooded with liquid nitrogen. However, there will be a further delay caused by the time required to cool the sample. The time required for a sample to reach a temperature can be estimated by the total heat to be removed from the sample divided by the rate of heat exchange using the algebraic formula:

$$t = (cm\Delta t_2) / [(kA\Delta t_1) / d]$$

in which t = the time required to cool the sample to a particular target temperature (s), c = specific heat of the material ($\text{J g}^{-1} \text{K}^{-1}$), m = the mass of material (g), k = thermal conductivity of the material ($\text{W m}^{-1} \text{K}^{-1}$), A = area of the exposed surface (m^2), d = distance the sample is from the surface (m), Δt_1 = driving temperature of coolant (K), and Δt_2 = the target temperature of the sample (K).

The thermal conductance of sapphire is high ($c = 13.0$, $m = 0.011$, $k = 23.1$, $A = 2.8 \times 10^{-5}$ area of the disk, $d = 10^{-4}$ m, $\Delta t_1 = -52^\circ\text{K}$, $\Delta t_2 = -32^\circ\text{K}$). If the chamber temperature were instantaneously -20°C , the temperature on the inner side of the 100-µm-thick sapphire disk should reach 0 °C in 0.01 ms.

The cells cultured on the sapphire disk are all within 5 µm of the surface in aqueous media ($c = 4.186$ specific heat for water, $m = 0.000141$ mass of water in the volume, $k = 0.56$ thermal conductivity of water, $A = 2.8 \times 10^{-5}$ area of the disk, $d = 5 \times 10^{-6}$ m distance from the surface, $\Delta t_1 = 54^\circ\text{K}$ assuming the chamber is at 253°K , and $\Delta t_2 = 34^\circ\text{K}$ is the target temperature of 273°K). This is of course an overestimate because it assumes that there is no cooling of the sample in the first 7 ms. The estimated time for specimens to reach 0 °C is 1.1 ms. Thus, the sample should reach 0 °C in less than 8.1 ms. Simulations of cooling using a differential equation for Fourier's law of heat conduction predicts that water 5 µm from the surface will reach 0 °C 5 ms after the chamber is flooded with liquid nitrogen, when a brass specimen holder is used in the Leica EMPact⁵². The telemetry reported that the chamber temperature drops to -20°C at 8 ms. However, because we cannot monitor the temperature of the sample, we have based our calculations on a target temperature for the chamber of -20°C , which comprises an 8 ms delay.

Thus, to freeze the sample 15 ms after light onset we performed the following protocol (Extended Data Fig. 2d). We fired a single light pulse at 0 ms, 7 ms after light onset we flooded the chamber with liquid nitrogen, 8 ms after application of liquid nitrogen the sample should reach 0 °C (the chamber temperature will be -20°C), so that the sample was frozen 15 ms after light onset. Action potentials are initiated 4.8 ms after light onset on average. Thus, the 15 ms freeze captures events that occurred 10.2 ms after the action potential on average. However these values should not be overinterpreted. There is a significant fluctuation in the initiation of the action potential after light onset, ranging from 3 to 9 ms, and in some cases an action potential fails altogether. The 15 ms time point probably represents events that occurred between 6 and 12 ms after the action potential. Specifying the exact temporal delay after an action potential is not appropriate—for any particular synapse we don't know precisely when the action potential occurred. For this reason we assign our temporal values to the arbitrary start point of light onset rather than tie it to a biological event such as action potential initiation.

After the freezing, the samples were transferred into cryovials containing 1% glutaraldehyde, 1% osmium tetroxide, 1% water and anhydrous acetone and processed in an automated freeze-substitution device (AFS2, Leica) with the following program: 2–5 h at -90°C , 5°C h^{-1} to -20°C , 12 h at 20°C , and 10°C h^{-1} to 20°C . Cells were stained en bloc with 0.1% uranyl acetate for 1 h, embedded in epon, and cured for 48 h in a 60°C oven. The samples were blinded before imaging and analysis. Serial 40 nm sections were collected on Formvar-coated (0.5%) single-slot grids, and 200 synaptic profiles were imaged using a Zeiss 902 electron microscope equipped with Megaview III camera. Based on the release probability in mouse hippocampal synapses and the preliminary data collected using a calcium-permeant variant of channelrhodopsin-2 (CaTCH), exocytosis and endocytosis would be captured in $\sim 30\%$ of synaptic profiles. Therefore, by collecting 200 profiles, we expected to observe at least 60 structures—sufficient to run statistical analysis. To assess ice crystal damage in the sample, we analysed the morphology of the mitochondria and synapses in each sample (Extended Data Fig. 9). We only collected images from tissues with no obvious ice crystal damage. Synaptic profiles were defined as boutons containing synaptic vesicles attached to a postsynaptic cell with a visible postsynaptic density. To sample unbiased populations of synapses, synaptic profiles were chosen randomly in regard to size or shape. Data were

collected from profiles in single sections rather than from reconstructed synapses. We analysed all data that had been collected.

The images were scored blind using an analysis program developed for ImageJ and Matlab (S.W., M.W.D. and E.M.J., unpublished). The active zones were defined as the portion of presynaptic membrane directly juxtaposed to the postsynaptic density. We defined docked vesicles as those contacting the plasma membrane and tethered vesicles as those with a visible tether and within 30 nm of the plasma membrane. Vesicles that lack tethers but are within 30 nm are defined as <30 nm. Tethers were visible for ~95% of the vesicles within 30 nm of plasma membrane. The diameter of vesicles was measured from the outer leaflet of membrane.

Collapsing vesicles decay with a time constant of 32 ms, but this value must be corrected because our data include a declining distribution of action potentials after the light stimulation ($\tau = 8$ ms). This value was calculated using the following formula:

We calculated the time constant for synaptic vesicle collapse. The presence of omega figures in our electron micrographs relies on the timing of action potentials after light stimulation and the speed of collapse of the synaptic vesicle. The presence of collapsing omega figures is then determined by the convolution of these two time constants:

$$e^{-t/\tau_1} \times e^{-t/\tau_2} = [1/(\tau_1 - \tau_2)] \times (e^{-t/\tau_1} - e^{-t/\tau_2})$$

in which t = time (ms), $\tau_1 = 8$ ms, time constant for action potential decay was determined from the distribution of action potentials, $\tau_2 = 20.3$ ms, time constant for vesicle collapse was determined as the best fit to the convolution.

For ferritin application, cells were immersed in solution containing ferritin (0.25 mg ml^{-1}) with a reduced concentration of calcium (1 mM) for 5 min to reduce ferritin uptake by spontaneous activity during incubation. Cells were then transferred into solution containing 4 mM calcium and 1 mM magnesium and frozen 100 ms after light stimulation. To improve the contrast of ferritin, specimens were not stained with uranyl acetate. In unstimulated cultures, 18% of the profiles exhibited some internalization of ferritin, of those profiles only 1 vesicle from the ~56 total vesicles contained ferritin.

For latrunculin-A and dynasore experiments, a solution containing 10 μM latrunculin-A or 80 μM dynasore or 0.1% DMSO was applied to cells 30 s before freezing. A single light pulse was applied 100 ms before the freeze of the latrunculin-A treated cells and both 100 ms and 1 s before the freeze of dynasore-treated cells. Following 30 s incubation with 80 μM dynasore, there was no significant increase in the total number of endocytic structures following the dynasore treatment. However, most of the large vesicles became trapped on the membrane. The necks were only visible in 10/57 large vesicles, probably due to the thickness of sections (40 nm).

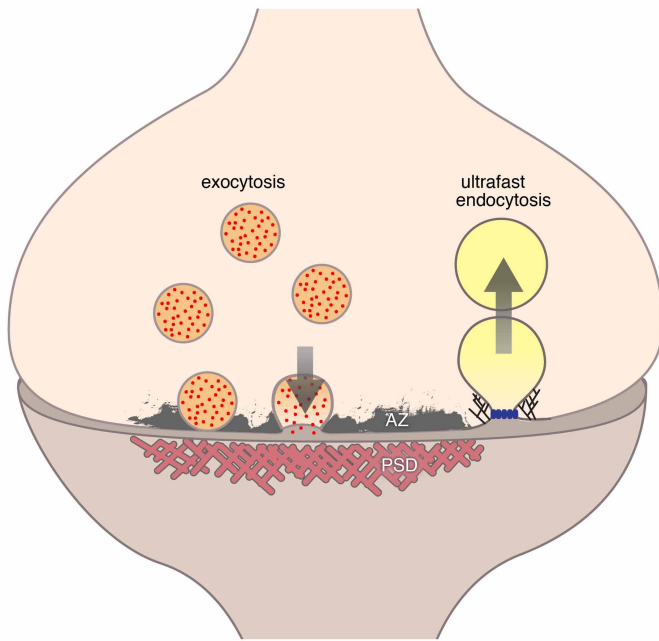
All the solutions used in these experiments contain 4 mM calcium and 30 μM bicuculline to increase the release probability and 3 μM NBQX to minimize the recurrent network activity.

Electron tomography. To acquire tilt series, serial 200-nm thick sections were cut and mounted on the Pioloform-coated (0.7%) single slot grids. Prior to image acquisition, 10 nm gold particles were deposited on both sides of grids by immersing the grids into solution containing gold particles at a density of $5.7 \times 10^{12} \text{ ml}^{-1}$ (<http://microspheres-nanospheres.com/>) for approximately 4 min. The gold particles are used as fiducial markers to align the tilt series. The grids are then loaded into the electron microscope (FEI TF20) equipped with a CCD camera (FEI Eagle 4K). Sections were stabilized under electron beam (200 kV) for 30 min before image acquisition. Tilt series from $+65^\circ$ to -65° were collected from 43 synapses chosen at random using Xplore3D software. Tomograms were generated using IMOD⁵³. Membranes were traced from every 10 virtual section in Amira or TrakEM2⁵⁴ using a Wacom pen tablet. The gaps were interpolated to prevent hand-tracing errors. The postsynaptic density was segmented using a Lasso tool.

Membrane calculations. To calculate the amount of membrane added to the surface by exocytosis, we determined the surface area of docked vesicles that fused after stimulation. The average number of docked vesicles was reduced from 1.7 (0 ms) to 1.0 (15 ms) vesicle per profile, thus 0.7 vesicles fused in each profile, assuming that no vesicles become docked in the first 15 ms. The diameter of a synaptic vesicle is 41.1 nm, and the surface area is ~5,300 nm^2 . Therefore, in each 40-nm section, 3,700 nm^2 is added to the surface area of the synaptic plasma membrane.

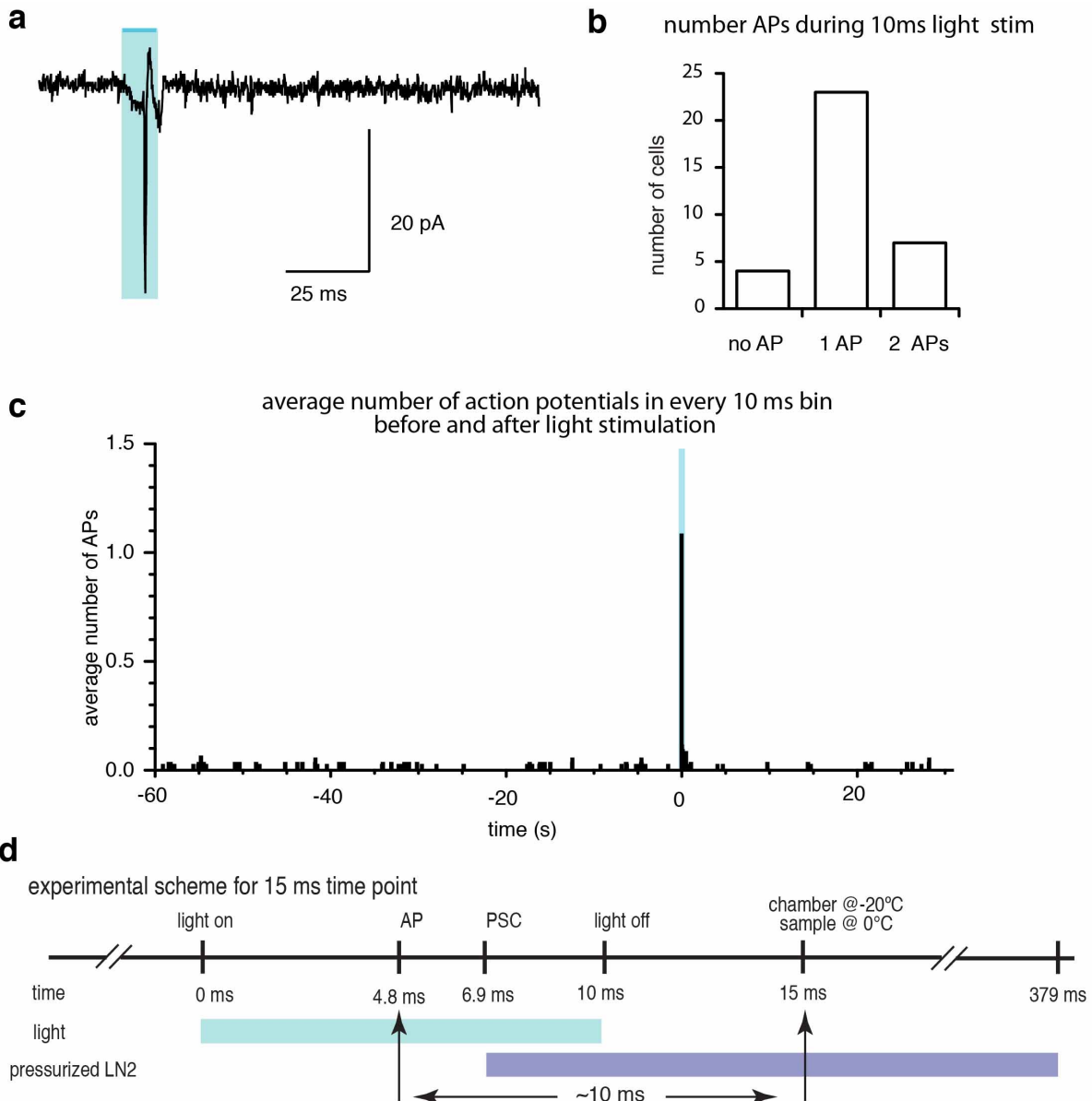
To calculate the amount of membrane retrieved, we determined the surface area of endocytic structures observed at 100 ms after stimulation, assuming that all the pits progress to 82 nm vesicles. The number of endocytic structures increased from 0.1 to 0.4, and thus the net increase was 0.3 endocytic structures per profile. However, the diameter of the large endocytic structures was 82 nm—twice as large as that of synaptic vesicles, and thus the chance of capturing such structures in a 40-nm section is twice as high. To estimate the amount of membrane recovered in a single 40-nm section, the number of endocytic structures was divided by 2. Therefore, for each synaptic profile, 0.15 large endocytic structures would be expected. Because the surface area of an 82 nm large vesicle was 21,000 nm^2 , the total amount of membrane retrieved from each profile is 3,150 nm^2 or 0.6 vesicle equivalent of membrane—roughly equal to the surface area added during exocytosis.

50. Lois, C., Hong, E. J., Pease, S., Brown, E. J. & Baltimore, D. Germline transmission and tissue-specific expression of transgenes delivered by lentiviral vectors. *Science* **295**, 868–872 (2002).
51. Rost, B. R. *et al.* Autaptic cultures of single hippocampal granule cells of mice and rats. *Eur. J. Neurosci.* **32**, 939–947 (2010).
52. Studer, D., Humbel, B. M. & Chiquet, M. Electron microscopy of high pressure frozen samples: bridging the gap between cellular ultrastructure and atomic resolution. *Histochem. Cell Biol.* **130**, 877–889 (2008).
53. Kremer, J. R., Mastrorarde, D. N. & McIntosh, J. R. Computer visualization of three-dimensional image data using IMOD. *J. Struct. Biol.* **116**, 71–76 (1996).
54. Cardona, A. *et al.* TrakEM2 software for neural circuit reconstruction. *PLoS ONE* **7**, e38011 (2012).



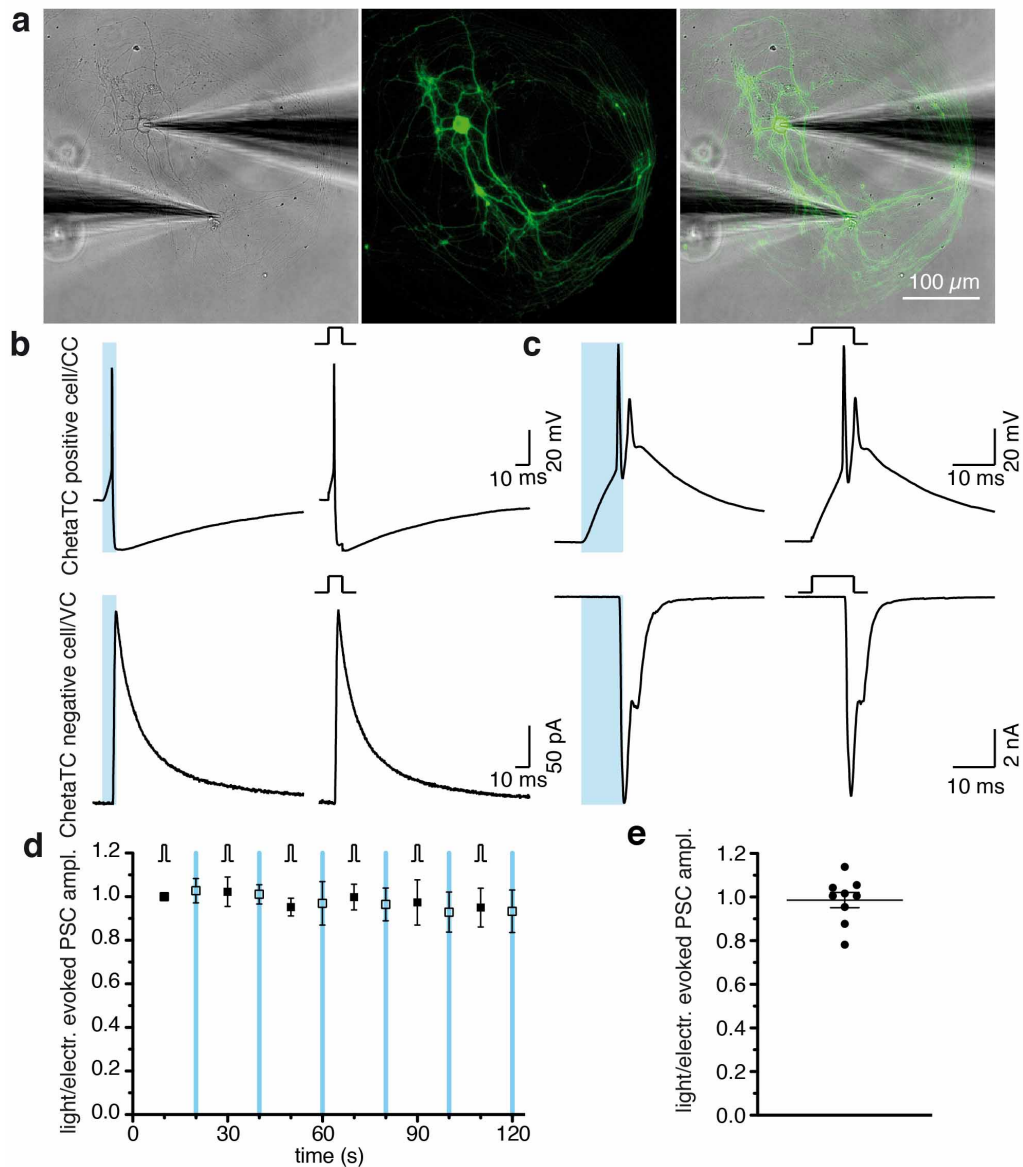
Extended Data Figure 1 | A schematic summarizing ultrafast endocytosis.

Exocytosis in the active zone is followed by rapid internalization of membrane at the edge of the active zone. Synaptic vesicles directly in contact with plasma membrane fuse about 2 ms after an action potential and collapse into membrane. Ultrafast endocytosis occurs at the edge of active zone within 100 ms after stimulation and is mediated by actin and dynamin. The endocytic structures are larger than synaptic vesicles. AZ, active zone; PSD, postsynaptic density.



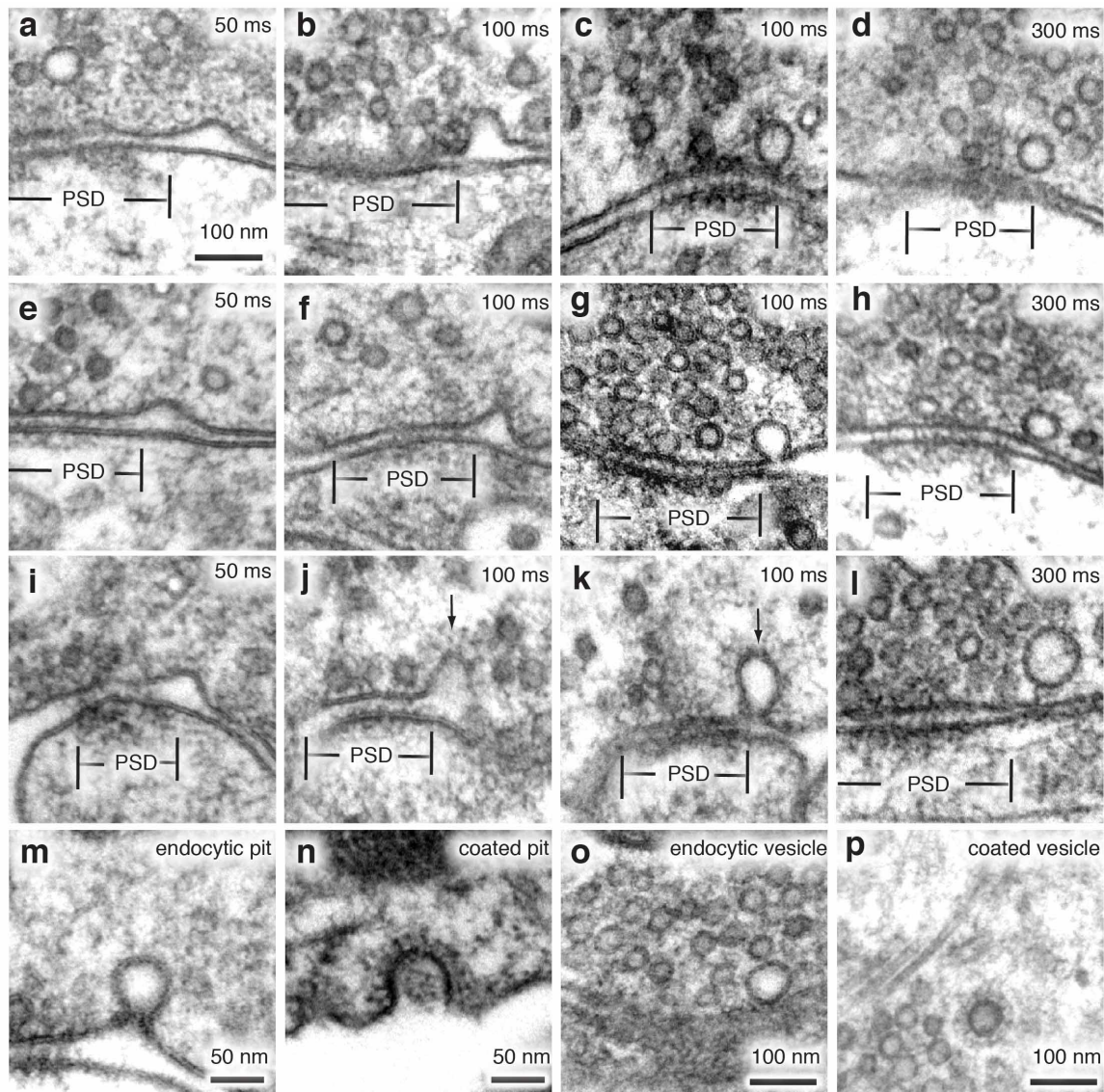
Extended Data Figure 2 | Channelrhodopsin induces action-potential-driven vesicle fusion. **a**, Cell-attached voltage clamp recordings of single light-evoked action potentials in presence of synaptic blockers NBQX and bicuculline. **b**, Number of action potentials triggered during the 10 ms light pulse. Most cells fired at least one action potential during the light pulse (88%, 30/34), though some cells did not respond to the light stimulus (12%, 4/34). Some cells fired a second action potential (26%, 7/34). **c**, A histogram showing the average number of action potentials at different time points before and after the light application. Each column is binned by 10 ms. Action potentials observed after

light-off are likely due to the spontaneous activity of cells. **d**, Freezing protocol for 15 ms samples. A single light pulse was fired at 0 ms. At 7 ms after light onset, the chamber was flooded with liquid nitrogen. At 8 ms after application of liquid nitrogen, the sample should reach 0 °C (when the chamber temperature is at -20 °C), so that the sample was frozen 15 ms after light onset. Action potentials are initiated 4.8 ms after light onset on average. Thus, the 15 ms freeze is capturing events that occurred on average 10.2 ms after the



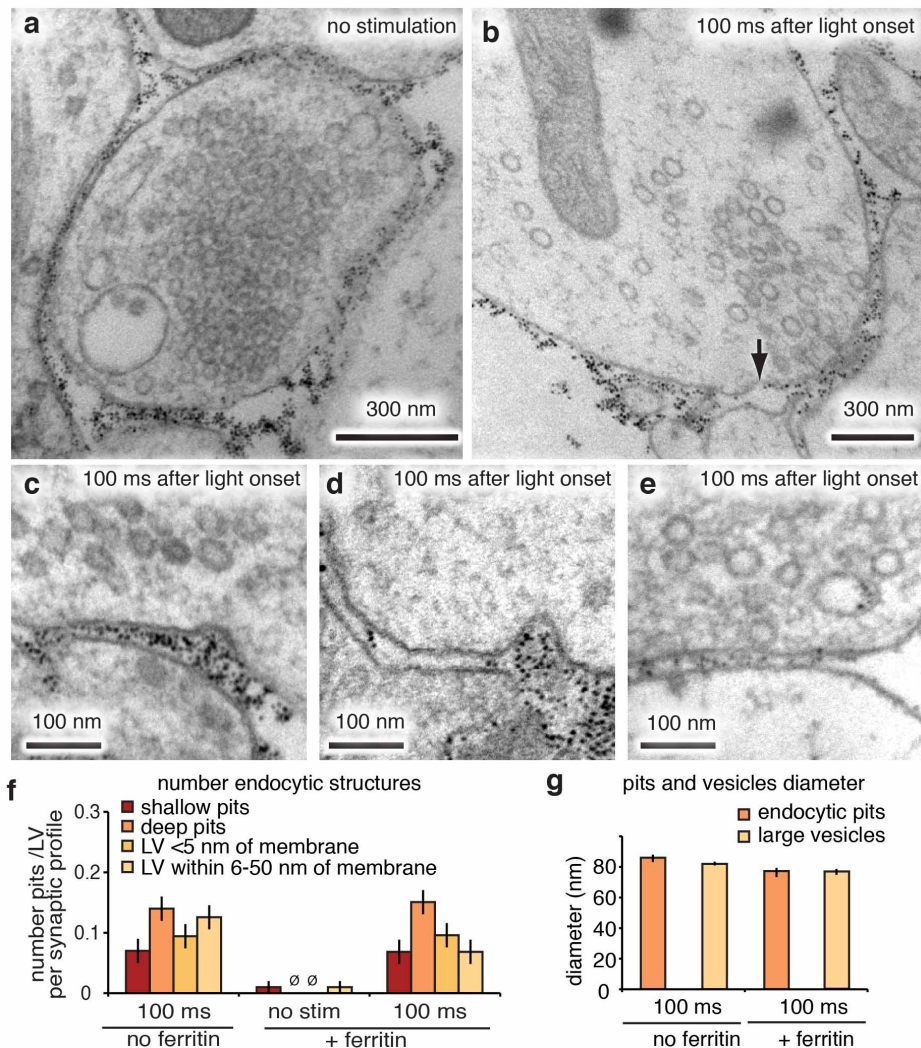
Extended Data Figure 3 | Light and electrical stimulation in the same cell elicit identical postsynaptic currents. **a**, Paired whole-cell recordings of ChetaTC-expressing (YFP) and non-expressing neurons that were co-cultured on small microislands of astrocytes. Action potentials were triggered every 10 s in the ChetaTC-positive cell by alternating between 10 ms current injection via the patch pipette and 10 ms light flashes. **b**, Example of a cell pair with a GABAergic ChetaTC-positive neuron. Presynaptic action potentials were recorded in current clamp (CC) of the ChetaTC-positive cell. Postsynaptic inhibitory postsynaptic currents (IPSCs) were recorded in voltage clamp (VC) from the non-infected neuron (bottom panel; holding potential -50 mV). **c**, Presynaptic action potentials and excitatory postsynaptic currents (EPSCs)

evoked by light or somatic depolarization in a pair of neurons with a glutamatergic ChetaTC-positive neuron. The postsynaptic cell was voltage-clamped at -70 mV . **d**, Time plot of postsynaptic responses triggered by alternating light-induced depolarization (blue bars/open symbols) and electrical stimulation (current step/closed symbols). Both EPSC and IPSC amplitudes were normalized to the first response evoked by electrical stimulation and pooled ($n = 9$). **e**, Scatter plot of postsynaptic currents evoked by ChetaTC stimulation normalized to direct electrical stimulation in the same neuron. Responses are not different for the two modes of action potential induction ($P = 0.77$, one sample t -test). Error bars, s.e.m.



Extended Data Figure 4 | Large invaginations adjacent to the active zone are endocytic intermediates. **a–l**, Additional representative micrographs showing shallow invaginations 50 ms after stimulation (**a, e, i**), deep invaginations 100 ms after stimulation (**b, c, f, g, j, k**) and large vesicles at the edge of active zone 300 ms after stimulation (**d, h, l**). **m, o**, Coats are usually absent on ultrafast

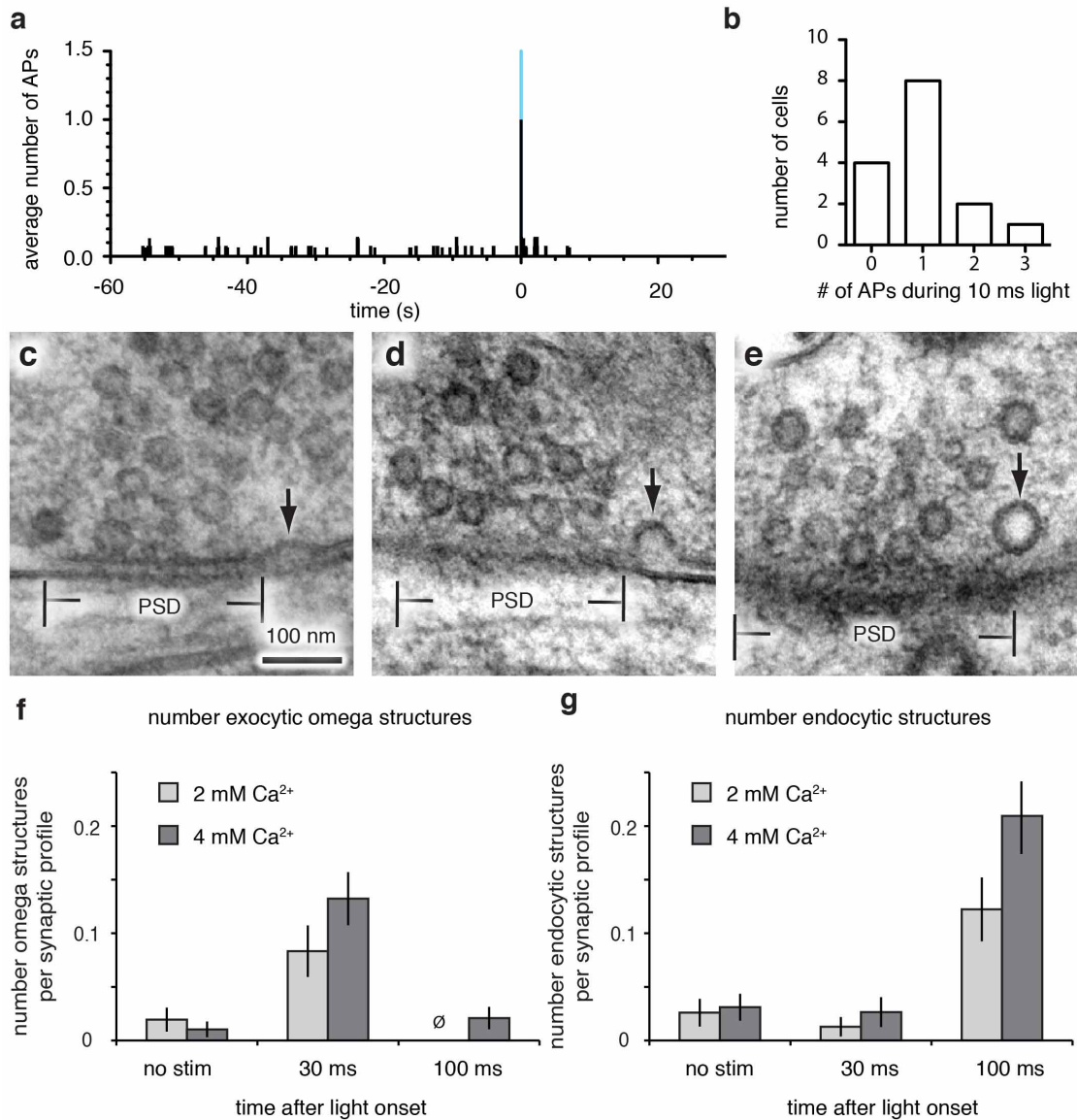
invaginations, but can occasionally be observed (**j, k**, arrow). **n, p**, But these differ from those observed at classical clathrin coated pits (**n**) or vesicles (**p**). The coated pit (**n**) was not observed at the synapse but was rather at the plasma membrane of soma.



Extended Data Figure 5 | Large invaginations take up a fluid phase marker.

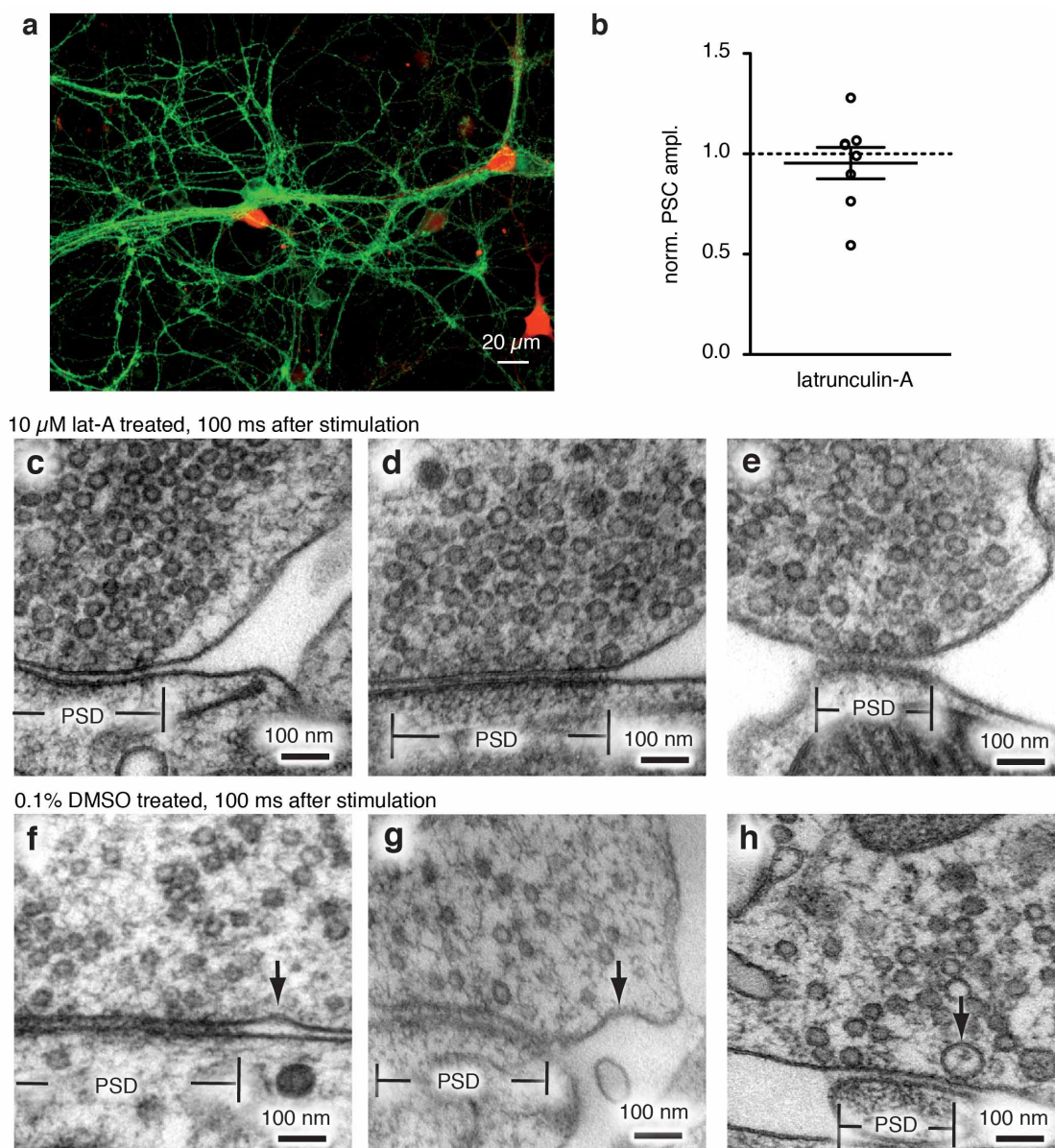
a–e, Additional representative micrographs showing ferritin uptake in the whole terminal in non-stimulation control (**a**) and 100 ms after stimulation (**b**) and by large structures at the edge of active zones 100 ms after stimulation (**c–e**). An arrow in **b** indicates a ferritin-positive shallow pit. Ferritin was applied to cells for 5 min before the light stimulation. Note that very little ferritin was internalized during the pre-incubation period, suggesting that the ferritin distribution is associated acutely with endocytosis after the stimulation. In unstimulated cultures, 18% of the profiles exhibited some internalization of ferritin; of those profiles only 1 vesicle from the ~56 total vesicles contained ferritin. At 100 ms, 26% of the profiles exhibited synaptic vesicles with ferritin ($P = 0.29$); of those profiles that had internalized ferritin only 1 vesicle from

51.2 total vesicles contained ferritin. Thus, ultrafast endocytosis did not directly generate detectable numbers of synaptic vesicles with ferritin. **f**, Number of shallow pits (<40 nm), deep pits (>40 nm), large vesicles associated with the membrane (<5 nm) and large vesicles associated with the plasma membrane (6–50 nm of the membrane) in controls and ferritin-containing seeded cultures. In ferritin seeded cultures the large vesicles near the membrane (within 5 nm) all contained ferritin. The total number of ferritin-positive endocytic structures was 0.38 ± 0.03 endocytic structures per profile, similar to the endocytosis values obtained in Fig. 3i without ferritin (0.43 ± 0.03 endocytic structures per profile). **g**, Diameter of large vesicles (86.0 ± 2.4 ; $n = 51$) and endocytic invaginations (77.3 ± 3 nm; $n = 16$; $P = 0.33$). ‘No ferritin’ controls are from the samples in Fig. 3. Error bars, s.e.m.



Extended Data Figure 6 | Ultrafast endocytosis occurs with similar dynamics in 2 mM and 4 mM extracellular calcium. **a**, A histogram showing the average number of action potentials at different time points before and after the light application in an external solution with 2 mM calcium. Each column is binned by 10 ms. Action potentials observed after light-off are probably due to spontaneous activity of cells. **b**, Average number of action potentials triggered during the 10 ms light pulse. An action potential was observed during the light pulse in 73% of the cells (11/15); 13% (2/15) fired a second action potential

within the 10 ms light pulse. No action potential was observed in 27% of the cells (4/15). **c–e**, Representative micrographs showing invaginations and large vesicles in the periactive zone at 100 ms after stimulation. **f, g**, Average number of exocytic pits (**f**) and endocytic structures (**g**) at 0 ms (no stim), 30 ms and 100 ms after stimulation in 2 mM calcium (light grey) and in 4 mM calcium (dark grey) conditions. Endocytic structures include shallow and deep pits summed. 4 mM data are from the samples in Figs 1 and 3. Error bars, s.e.m.

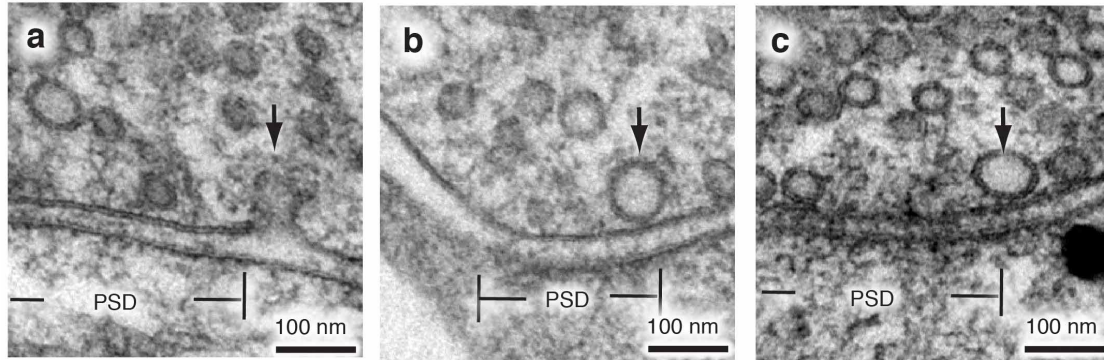


Extended Data Figure 7 | Ultrafast endocytosis is mediated by actin.

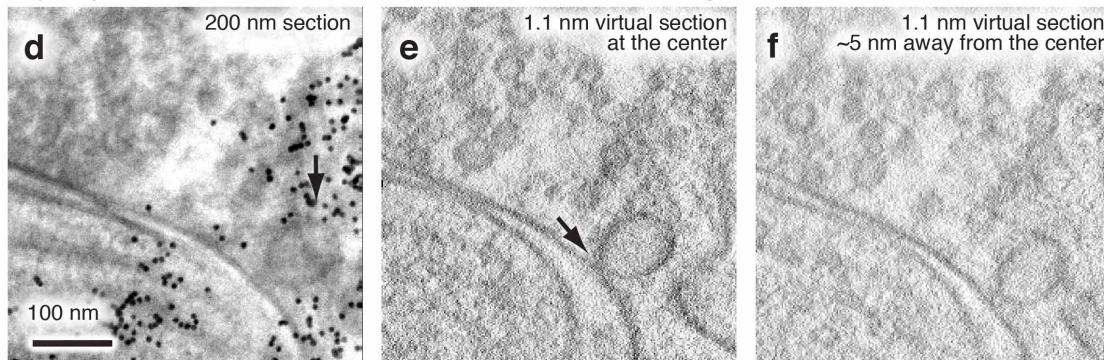
a, Electrophysiological recordings on mixed cultures. PSCs were recorded from ChetaTC-negative neurons (red fluorescence) while stimulating ChetaTC/YFP-positive neurons with light. **b**, Scatter plot of postsynaptic currents evoked by channelrhodopsin stimulation in 10 μ M latrunculin-A/0.1% DMSO normalized to postsynaptic currents in 0.1% DMSO in the same neuron. 30 s incubation with latrunculin-A has no effect on evoked

neurotransmission. Average PSC amplitudes were normalized to average PSC amplitudes preceding latrunculin-A application ($n = 8$, normalized PSC in latrunculin-A is 0.95 ± 0.08 , $P = 0.6$, one sample t -test). **c–h**, Additional representative micrographs showing 10 μ M latrunculin-A-treated (**c–e**) and 0.1% DMSO-treated (**f–h**) cells 100 ms after stimulation. Ultrafast endocytosis occurs in DMSO-treated cells but is completely blocked in latrunculin-A treated cells. Error bar, s.e.m.

80 μ M Dynasore treated, 1 s after stimulation, 40-nm thick section

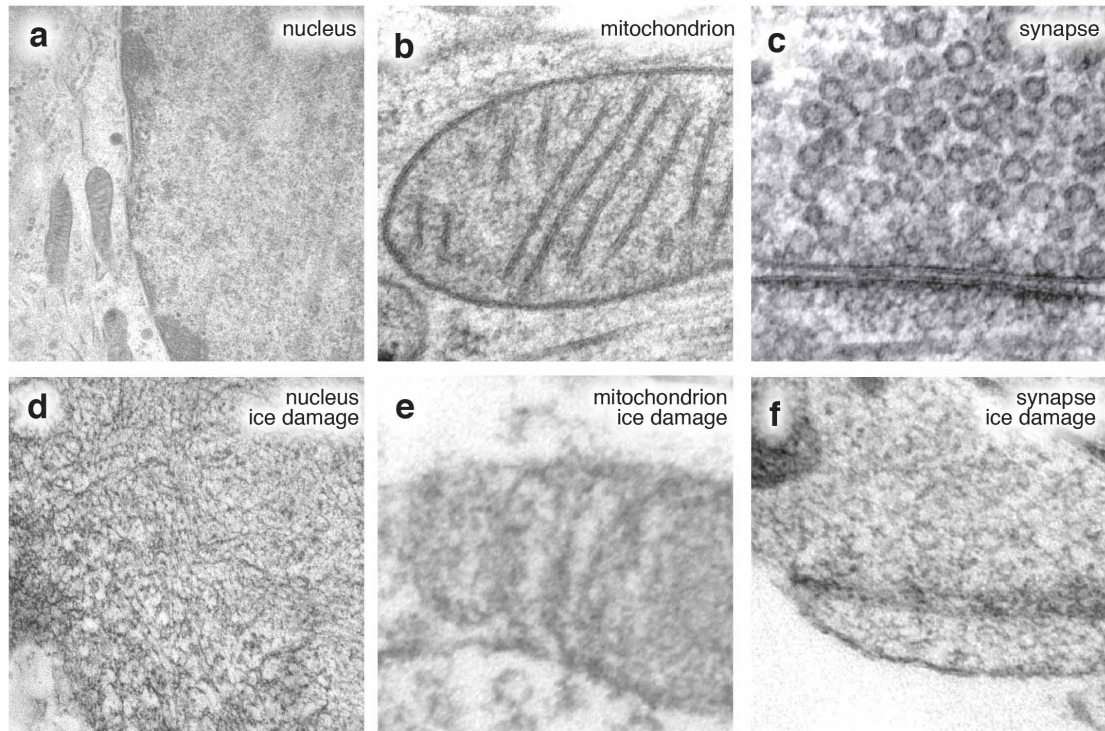


80 μ M Dynasore treated, 1 s after stimulation, 200-nm thick section tomogram



Extended Data Figure 8 | Ultrafast endocytosis is mediated by dynamin.
a–f, Additional representative micrographs showing 80 μ M dynasore-treated cells from 40-nm thick sections (**a–c**) and a 200-nm tomogram (**d–f**). Ultrafast endocytic structures are trapped on the surface in the dynasore-treated cells. Note that large vesicles are found associated with

the membrane (**a–c**, **d**, **f**) but the necks of the trapped structures are only visible at their centre (**a**, **e**) due to the thickness of the sections. Electron tomography was performed on 21 sections (200-nm thick). 9 out of 21 tomograms showed a trapped structure, and all of these trapped structures were connected to the membrane at their centre.



Extended Data Figure 9 | Ice crystal damage was not observed in cell cultures subjected to high pressure freezing. a–f, Sample micrographs show a nucleus (a, d), a mitochondrion (b, e), and a synapse (c, f). a–c, In these samples there is no visible damage by ice crystals. d–f, Samples exhibiting ice crystal

damage caused by brief accidental removal from liquid nitrogen. Note the reticulated appearance caused by protein aggregation. Ice damage was not observed in the samples used in this study.

Supplementary Table 1.

For statistical comparisons for diameters of vesicles and pits, *p*-values were calculated using Student's *t*-test. For number of vesicles and pits, we used Mann-Whitney U tests because of the skewed distribution of the data. The skewness was determined using Pearson's skewness test. The confidence level was set at 0.05 in each case. For Fig. 1f, 2c, 2d, and 3i, we applied the Bonferroni correction to reduce the chance of obtaining false positive in multiple comparisons on a single dataset. Therefore, the confidence level is 0.006 in those cases. The gray shade in the P-value columns suggest the difference observed is statistically significant.

Number of vesicles and pits in Channelrhodopsin transfected cells

	No stimulation		No Chr2 100 ms		
N (synaptic profiles)	193		174		
	Mean	SEM	Mean	SEM	P value
Exocytic pits (Fig.1f)	0.01	0.01	0.03	0.01	0.12
Docked vesicles (Fig. 2c)	1.7	0.1	1.7	0.1	0.58
Tethered vesicles (Fig. 2d)	2.2	0.1	2	0.1	0.08
Shallow endocytic pits (Fig. 3i)	0.02	0.01	0.02	0.01	0.88
Deep endocytic pits (Fig. 3i)	0.01	0.01	0.02	0.01	0.34
Large vesicles (Fig. 3i)	0.06	0.01	0.05	0.01	0.68

	No stimulation		15 ms		
N (synaptic profiles)	193		193		
	Mean	SEM	Mean	SEM	P value
Exocytic pits (Fig.1f)	0.01	0.01	0.19	0.03	<.0001
Docked vesicles (Fig. 2c)	1.7	0.1	1	0.1	<.0001
Tethered vesicles (Fig. 2d)	2.2	0.1	2.1	0.1	0.26
Shallow endocytic pits (Fig. 3i)	0.02	0.01	0.01	0.01	0.18
Deep endocytic pits (Fig. 3i)	0.01	0.01	0	0.01	0.57
Large vesicles (Fig. 3i)	0.06	0.01	0.07	0.01	0.68

	No stimulation		30 ms		
N (synaptic profiles)	193		189		
	Mean	SEM	Mean	SEM	P value

Exocytic pits (Fig.1f)	0.01	0.01	0.13	0.02	<.0001
Docked vesicles (Fig. 2c)	1.7	0.1	1	0.1	<.0001
Tethered vesicles (Fig. 2d)	2.2	0.1	2.2	0.1	0.67
Shallow endocytic pits (Fig. 3i)	0.02	0.01	0.01	0.01	0.43
Deep endocytic pits (Fig. 3i)	0.01	0.01	0.01	0.01	0.63
Large vesicles (Fig. 3i)	0.06	0.01	0.07	0.01	0.78

	No stimulation		50 ms		
N (synaptic profiles)	193		191		
	Mean	SEM	Mean	SEM	P value
Exocytic pits (Fig.1f)	0.01	0.01	0.05	0.02	0.03
Docked vesicles (Fig. 2c)	1.7	0.1	0.9	0.1	<.0001
Tethered vesicles (Fig. 2d)	2.2	0.1	2.4	0.1	0.49
Shallow endocytic pits (Fig. 3i)	0.02	0.01	0.13	0.01	<.0001
Deep endocytic pits (Fig. 3i)	0.01	0.01	0.04	0.01	0.05
Large vesicles (Fig. 3i)	0.06	0.01	0.1	0.01	0.18

	No stimulation		100 ms		
N (synaptic profiles)	193		191		
	Mean	SEM	Mean	SEM	P value
Exocytic pits (Fig.1f)	0.01	0.01	0.02	0.01	0.4
Docked vesicles (Fig. 2c)	1.7	0.1	1	0.1	<.0001
Tethered vesicles (Fig. 2d)	2.2	0.1	2.2	0.1	0.92
Shallow endocytic pits (Fig. 3i)	0.02	0.01	0.07	0.02	0.01
Deep endocytic pits (Fig. 3i)	0.01	0.01	0.14	0.02	<.0001
Large vesicles (Fig. 3i)	0.06	0.01	0.22	0.02	<.0001

	No stimulation		300 ms		
N (synaptic profiles)	193		188		
	Mean	SEM	Mean	SEM	P value
Exocytic pits (Fig.1f)	0.01	0.01	0.04	0.02	0.14
Docked vesicles (Fig. 2c)	1.7	0.1	1	0.1	<.0001
Tethered vesicles (Fig. 2d)	2.2	0.1	2.6	0.1	0.01
Shallow endocytic pits (Fig. 3i)	0.02	0.01	0.02	0.02	0.74

3i)					
Deep endocytic pits (Fig. 3i)	0.01	0.01	0.04	0.01	0.05
Large vesicles (Fig. 3i)	0.06	0.01	0.16	0.01	0.002

	No stimulation		1 s		
N (synaptic profiles)	193		179		
	Mean	SEM	Mean	SEM	P value
Exocytic pits (Fig. 1f)	0.01	0.01	0.07	0.02	0.002
Docked vesicles (Fig. 2c)	1.7	0.1	1.2	0.1	<.0001
Tethered vesicles (Fig. 2d)	2.2	0.1	2	0.1	0.18
Shallow endocytic pits (Fig. 3i)	0.02	0.01	0.07	0.02	0.02
Deep endocytic pits (Fig. 3i)	0.01	0.01	0.11	0.02	<.0001
Large vesicles (Fig. 3i)	0.06	0.01	0.13	0.01	0.03

	No stimulation		3 s		
N (synaptic profiles)	193		189		
	Mean	SEM	Mean	SEM	P value
Exocytic pits (Fig. 1f)	0.01	0.01	0.02	0.01	0.4
Docked vesicles (Fig. 2c)	1.7	0.1	1.3	0.1	0.003
Tethered vesicles (Fig. 2d)	2.2	0.1	1.8	0.1	0.003
Shallow endocytic pits (Fig. 3i)	0.02	0.01	0.02	0.01	0.73
Deep endocytic pits (Fig. 3i)	0.01	0.01	0.04	0.01	0.09
Large vesicles (Fig. 3i)	0.06	0.01	0.08	0.01	0.5

	No stimulation		10 s		
N (synaptic profiles)	193		178		
	Mean	SEM	Mean	SEM	P value
Exocytic pits (Fig. 1f)	0.01	0.01	0.04	0.02	0.07
Docked vesicles (Fig. 2c)	1.7	0.1	1.6	0.1	0.37
Tethered vesicles (Fig. 2d)	2.2	0.1	1.8	0.1	0.007
Shallow endocytic pits (Fig. 3i)	0.02	0.01	0.03	0.01	0.44
Deep endocytic pits (Fig. 3i)	0.01	0.01	0.01	0.01	0.94
Large vesicles (Fig. 3i)	0.06	0.01	0.06	0.01	0.99

Number of vesicles and pits in Munc13 DKO

	Munc13 DKO No stimulation		Munc13 DKO 30 ms		
N (synaptic profiles)	151		139		
	Mean	SEM	Mean	SEM	P value
Exocytic pits	0	0	0	0	N/A
Docked vesicles	0.1	0.03	0.1	0.03	0.68
Tethered vesicles	2.2	0.2	3	0.2	<.0001
Shallow endocytic pits (Fig. 3j)	0.01	0.01	0.01	0.01	0.95
Deep endocytic pits (Fig. 3j)	0	0	0	0	N/A
Large vesicles (Fig. 3j)	0.04	0.003	0.06	0.005	0.48

	Munc13 DKO No stimulation		Munc13 DKO 100 ms		
N (synaptic profiles)	151		140		
	Mean	SEM	Mean	SEM	P value
Exocytic pits	0	0	0	0	
Docked vesicles	0.1	0.03	0.1	0.02	0.22
Tethered vesicles	2.2	0.2	2.5	0.2	0.22
Shallow endocytic pits (Fig. 3j)	0.01	0.01	0	0	N/A
Deep endocytic pits (Fig. 3j)	0	0	0	0	N/A
Large vesicles (Fig. 3j)	0.04	0.003	0.06	0.005	0.35

Number of endocytic structures in tomograms

Fig. 4c	50 ms		100 ms		
N (tomograms)	8		35		
	Mean	SEM	Mean	SEM	P value
Shallow endocytic pits	0.41	0.13	0.17	0.06	
Deep endocytic pits	0.06	0.06	0.26	0.08	
LV <50 nm of memb	0.06	0.06	0.17	0.06	

Number of pits in Latrunculin-treated cells

Fig. 5e	No drug		0.1% DMSO		
N (synaptic profiles)	193		178		
	Mean	SEM	Mean	SEM	P value

Exocytic pits	0.02	0.01	0.06	0.02	0.12
Endocytic pits	0.21	0.03	0.17	0.03	0.41

Fig. 5e	No drug		10 μ M Latrunculin-a		
N (synaptic profiles)	193		185		
	Mean	SEM	Mean	SEM	P value
Exocytic pits	0.02	0.01	0.02	0.01	0.97
Endocytic pits	0.21	0.03	0	0	<.0001

Number of endocytic structures in dynasore-treated cells

Fig. 5f	control 0 ms		80 μ M Dynasore 0 ms		
N (synaptic profiles)	193		53		
	Mean	SEM	Mean	SEM	P value
Shallow endocytic pits	0.02	0.01	0.02	0.01	0.94
Deep endocytic pits	0.01	0.01	0.02	0.01	0.62
LV <5 nm of memb	0.02	0.01	0.04	0.01	0.48
LV <6-50 nm of memb	0.04	0.01	0.04	0.01	0.91

Fig. 5f	control 100 ms		80 μ M Dynasore 100 ms		
N (synaptic profiles)	191		50		
	Mean	SEM	Mean	SEM	P value
Shallow endocytic pits	0.07	0.02	0.06	0.03	0.75
Deep endocytic pits	0.14	0.02	0.16	0.04	0.67
LV <5 nm of memb	0.09	0.02	0.16	0.04	<.0001
LV <6-50 nm of memb	0.13	0.01	0.04	0.01	0.08

Fig. 5f	control 1 s		80 μ M Dynasore 1 s		
N (synaptic profiles)	179		223		
	Mean	SEM	Mean	SEM	P value
Shallow endocytic pits	0.07	0.02	0.08	0.02	0.94

Deep endocytic pits	0.11	0.02	0.08	0.02	0.38
LV <5 nm of memb	0.06	0.02	0.22	0.03	<.0001
LV <6-50 nm of memb	0.06	0.02	0.03	0.01	0.09

Number of ferritin-positive endocytic structures

Supplementary Fig. 5f	No ferritin 100 ms		ferritin 100 ms		
N (synaptic profiles)	191		73		
	Mean	SEM	Mean	SEM	P value
Shallow endocytic pits	0.07	0.02	0.07	0.02	
Deep endocytic pits	0.14	0.02	0.15	0.02	
LV <5 nm of memb	0.09	0.02	0.1	0.02	
LV <6-50 nm of memb	0.13	0.01	0.07	0.02	

Supplementary Fig. 5f	Ferritin no stim		ferritin 100 ms		
N (synaptic profiles)	100		73		
	Mean	SEM	Mean	SEM	P value
Shallow endocytic pits	0.01	0.01	0.07	0.02	
Deep endocytic pits	0	0	0.15	0.02	
LV <5 nm of memb	0	0	0.1	0.02	
LV <6-50 nm of memb	0.01	0.01	0.07	0.02	

Number of exocytic or endocytic pits in 2 mM calcium

2 mM calcium	No stimulation		30 ms		100 ms	
N (synaptic profiles)	193		174		174	
	Mean	SEM	Mean	SEM	Mean	SEM
Exocytic pits	0.02	0.01	0.08	0.02	0	0
Endocytic pits	0.03	0.01	0.01	0.01	0.12	0.03

Diameter of vesicles and pits

Fig. 1g	Synaptic vesicles	Exocytic pits	P value
Mean	41.1	40.9	0.71
SEM	0.09	1.16	

Fig. 3h	Large vesicles	Endocytic pits	P value
Mean	82.03	86.02	0.33
SEM	1.2	2.4	

Fig. 4d	Large vesicles	Endocytic pits	P value
Mean	78	76.3	0.56
SEM	3.3	1.9	

Supplementary Fig. 5g	No ferritin 100 ms		
	N	Mean	SEM
Endocytic pits diameter	40	76.7	1.9
LV diameter	572	82	1.2
	ferritin 100 ms		
	N	Mean	SEM
Endocytic pits diameter	16	77.3	3
LV diameter	51	86	2.4